An Assessment of Multimodel Simulations for the Variability of Western North Pacific Tropical Cyclones and Its Association with ENSO

RONGQING HAN,[a] HUI WANG,[b] ZENG-ZHEN HU,[b] ARUN KUMAR,[b] WEIJING LI,[a] LINDSEY N. LONG,[b,c] JAE-KYUNG E. SCHEMM,[b] PEITAO PENG,[b] WANQIU WANG,[b] DONG SI,[a] XIAOLONG JIA,[a] MING ZHAO,[d] GABRIEL A. VECCHI,[d] TIMOTHY E. LAROW,[e] YOUNG-KWON LIM,[f,g] SIEGFRIED D. SCHUBERT,[f] SUZANA J. CAMARGO,[h] NAOMI HENDERSON,[h] JEFFREY A. JONAS,[i,j] AND KEVIN J. E. WALSH[k]

[a] *National Climate Center, China Meteorological Administration, Beijing, China*
[b] *NOAA/NWS/NCEP/Climate Prediction Center, College Park, Maryland*
[c] *Innovim, Greenbelt, Maryland*
[d] *NOAA/Geophysical Fluid Dynamics Laboratory, Princeton, New Jersey*
[e] *Center for Ocean-Atmospheric Prediction Studies, Florida State University, Tallahassee, Florida*
[f] *Global Modeling and Assimilation Office, NASA Goddard Space Flight Center, Greenbelt, Maryland*
[g] *Goddard Earth Sciences Technology and Research, I. M. Systems Group, Greenbelt, Maryland*
[h] *Lamont-Doherty Earth Observatory, Columbia University, Palisades, New York*
[i] *Center for Climate System Research, Columbia University, New York, New York*
[j] *NASA Goddard Institute for Space Studies, New York, New York*
[k] *School of Earth Sciences, University of Melbourne, Parkville, Victoria, Australia*

(Manuscript received 6 October 2015, in final form 5 April 2016)

ABSTRACT

An assessment of simulations of the interannual variability of tropical cyclones (TCs) over the western North Pacific (WNP) and its association with El Niño–Southern Oscillation (ENSO), as well as a subsequent diagnosis for possible causes of model biases generated from simulated large-scale climate conditions, are documented in the paper. The model experiments are carried out by the Hurricane Work Group under the U.S. Climate Variability and Predictability Research Program (CLIVAR) using five global climate models (GCMs) with a total of 16 ensemble members forced by the observed sea surface temperature and spanning the 28-yr period from 1982 to 2009. The results show GISS and GFDL model ensemble means best simulate the interannual variability of TCs, and the multimodel ensemble mean (MME) follows. Also, the MME has the closest climate mean annual number of WNP TCs and the smallest root-mean-square error to the observation.

Most GCMs can simulate the interannual variability of WNP TCs well, with stronger TC activities during two types of El Niño—namely, eastern Pacific (EP) and central Pacific (CP) El Niño—and weaker activity during La Niña. However, none of the models capture the differences in TC activity between EP and CP El Niño as are shown in observations. The inability of models to distinguish the differences in TC activities between the two types of El Niño events may be due to the bias of the models in response to the shift of tropical heating associated with CP El Niño.

1. Introduction

The distinct modulation of global tropical cyclone (TC) activity by the El Niño–Southern Oscillation (ENSO) has received much attention in the past three decades. For example, in the western North Pacific (WNP), with the highest fraction of the global annual mean number of TCs (Camargo et al. 2005), the phase of ENSO is one of the most important climate factors affecting the genesis, tracks, durations, landfall numbers, and intensities of TCs (e.g., Lander 1994; Chan 2000; Wang and Chan 2002; Chia and Ropelewski 2002; Camargo and Sobel 2005; Chen et al. 2006; Camargo et al. 2007b; Chen and Tam 2010; Hong et al. 2011; Kim

Corresponding author address: Dr. Hui Wang, NOAA/Climate Prediction Center, 5830 University Research Court, NCWCP, College Park, MD 20740.
E-mail: hui.wang@noaa.gov

DOI: 10.1175/JCLI-D-15-0720.1

et al. 2011; Ha et al. 2013; Wang et al. 2013; Zhang and Guan 2014). ENSO affects WNP TC activity by altering the large-scale flow pattern. The increase of the low-level shear vorticity generated by El Niño–induced low-level equatorial westerly anomalies favors more TC formation in the southeastern part of the WNP, while the upper-level convergence induced by the deepening of the East Asian trough and strengthening of the WNP subtropical high suppresses the TC formation in the northwestern part of the WNP, both resulting from El Niño forcing. The opposite is true for La Niña years (Wang and Chan 2002).

In recent years, it has come to be distinctly appreciated by the climate research and prediction community that there is diversity in the El Niño phenomenon (Capotondi et al. 2015). In particular, the extent to which the warmest equatorial Pacific sea surface temperature (SST) anomalies are principally in the central or eastern equatorial Pacific differs between different El Niño events and leads to distinct climate teleconnections (e.g., Larkin and Harrison 2005; Ashok et al. 2007; Takahashi et al. 2011; Hu et al. 2012; Wang et al. 2014; Capotondi et al. 2015). Although the zonal position of warmest SST anomalies during El Niño spans a continuum (Takahashi et al. 2011; Capotondi et al. 2015), it can be useful to explore extremes in that continuum to gain understanding of the mechanisms behind and the impacts of this rich spectrum of variability. On one extreme are El Niño events whose main anomalies are principally in the eastern equatorial Pacific, which are usually referred to as ''east Pacific (EP)'' or ''canonical'' El Niño events (e.g., Larkin and Harrison 2005). At the other extreme are events whose main warm SST anomalies are concentrated in the central Pacific, near the date line, which will be referred to here as ''central Pacific (CP) El Niño,'' but have elsewhere been referred to by many other names, including ''dateline El Niño events'' (Larkin and Harrison 2005), ''El Niño Modoki'' (Ashok et al. 2007; Yeh et al. 2009), and ''warm-pool ENSO'' (Kug et al. 2009; Hu et al. 2012). The zonal difference of the warmest SST anomalies is associated with distinct atmospheric convective heating anomalies and consequent changes in the atmospheric response around the globe (Larkin and Harrison 2005; Ashok and Yamagata 2009; Kao and Yu 2009; Hu et al. 2012).

The zonal position of maximum SST anomalies during El Niño has been shown to affect the impact of El Niño on tropical cyclone activity in the Atlantic (e.g., Kim et al. 2009; Wang et al. 2014). The focus of the present paper is on the WNP. Using observational data, Kim et al. (2011) noted distinct differences in WNP TC activity associated with the three phases of ENSO. In EP El Niño, the genesis and track density of TCs tend to be enhanced over the southeastern part of the WNP by the extension of the monsoon trough and weak wind shear over the central Pacific and suppressed in the northwestern part of the WNP by the strong westerly wind shear. In CP El Niño, with the westward shift of the warm SST forcing, the TC activity shifts toward the west and extends through the northwestern part of the WNP associated with the anomalous westerly wind and monsoon trough over the northwestern part of the WNP. In La Niña, the anomalous TC activity and large-scale circulations show almost a mirror image of the EP El Niño.

There is substantial skill in predicting seasonal TC activity over various basins using dynamical models (e.g., Zhao et al. 2010; Chen and Lin 2011, 2013; Vecchi et al. 2014). Although the interannual variability in some aspects of TC behavior could be estimated by the type of ENSO, the capability of global climate models (GCMs) in simulating the spatial distribution of the TC activity associated with the different phases of ENSO is still considered one of the key issues in dynamical seasonal prediction of TCs. In terms of the routine seasonal forecasts of TC frequency in the WNP, both the model simulations and real-time predictions using high-resolution GCMs in recent years are promising (Zhao et al. 2009, 2010; Chen and Lin 2011, 2013; Shaevitz et al. 2014; Vecchi et al. 2014; Wang et al. 2014; Mei et al. 2015; Murakami et al. 2015; Walsh et al. 2015), although statistical methods (e.g., Chan et al. 1998; Fan and Wang 2009; Yonekura and Hall 2011) and the dynamical–statistical combined approach (Wang et al. 2009; Kim et al. 2012; Li et al. 2013) have also been used in the past with some skill.

It is well recognized that high-resolution GCMs are capable of simulating TC activity more accurately than low-resolution models because of a better representation of the spatial scale of TCs (e.g., Camargo et al. 2005; Chauvin et al. 2006; Scoccimarro et al. 2011). For example, using the Geophysical Fluid Dynamics Laboratory (GFDL) GCM with a 50-km resolution and observed SSTs as boundary conditions, Zhao et al. (2009) simulated the annual mean counts of TCs in the Atlantic and the east, west, and South Pacific well, with correlations to observations being 0.8, 0.6, 0.5, and 0.3, respectively. The simulated 25-yr trend in Northern Hemisphere basinwide frequency for the period of 1981–2005 is also consistent with the observations. Although previous studies have examined simulations of WNP TCs using high-resolution GCMs, they emphasize the capability of a single GCM simulating TCs (Zhao et al. 2009; Chen and Lin 2011, 2013; Mei et al. 2015; Vecchi et al. 2014; Murakami et al. 2015) or an ensemble of simulations of TCs without considering specifically the forcing from the different types of ENSO (Shaevitz et al. 2014). There is a more complex relationship between SSTs and other environmental factors related to TCs in the WNP than in the

TABLE 1. List of five GCMs for the HWG interannual experiments, the number of ensemble members, model data grid, and references for TC tracking algorithms.

Model	Ensemble members	Model data grid points (zonal × meridional)	Tracking algorithm
FSU	3	384 × 192	LaRow et al. (2008)
GFDL	3	576 × 360	Zhao et al. (2009)
GISS	3	360 × 180	Camargo and Zebiak (2002)
GSFC	2	576 × 361	LaRow et al. (2008)
GFS	5	360 × 181	Camargo and Zebiak (2002)

Atlantic (Emanuel 2007). Therefore, it is necessary to evaluate the overall performance of multiple GCMs in simulating the response of WNP TCs to ENSO, then verify whether the simulations in the WNP can be as good as those in the North Atlantic (Wang et al. 2014) and explore possible causes of model biases in simulating the large-scale circulation associated with TCs. The assessment is based on the analysis of the Atmospheric Model Intercomparison Project (AMIP)–type simulations with five GCMs and comparisons with observations. The study aims to provide insights into the basic characteristics of WNP TC activity associated with different types of ENSO in GCMs.

Similar to Wang et al. (2014), the present study is based on the interannual experiment set of TC simulations performed by the Hurricane Working Group (HWG) with high-resolution atmospheric GCMs (Walsh et al. 2015), but focuses on WNP TC activity and its association with ENSO. This paper is organized as follows. Section 2 provides a brief description of data, models, and analysis methods being used. Section 3 characterizes WNP TC activity and its association with ENSO in observations. The performance of GCMs in simulating the variability of WNP TCs and its association with ENSO is assessed in section 4. Some possible explanations for the differences between the models and observations are explored in section 5. Conclusions are given in section 6.

2. Data and models

The data used in this study consist of SST, WNP TC tracks, precipitation, 500-hPa relative humidity, and 200-, 500-, and 850-hPa winds over a 28-yr (1982–2009) period from both observations and simulations with five atmospheric GCMs. All data are the same as used by Wang et al. (2014), except for the observed TC track density and origin data from the Regional Specialized Meteorological Center (RSMC) Tokyo–Typhoon Center best-track dataset (available online at http://www.jma.go.jp/jma/jma-eng/jma-center/rsmc-hp-pub-eg/trackarchives.html). The RSMC dataset has a high reliability in terms of annual frequency, track location, and intensity of TCs since the 1980s (Ren et al. 2011).

The observed time-varying SSTs were used as common forcing to drive different models, which are from the Hadley Centre Sea Ice and Sea Surface Temperature (HadISST) dataset (Rayner et al. 2003) in monthly averages and with a horizontal resolution of 1° × 1° (latitude × longitude), except for the Florida State University (FSU) model forced with the NOAA Optimum Interpolation SST version 2 (OISSTv2; Reynolds et al. 2002). The rainfall dataset is the Climate Prediction Center (CPC) Merged Analysis of Precipitation (CMAP; Xie and Arkin 1997). The variables describing the atmospheric circulation, including relative humidity and horizontal winds, are obtained from the National Centers for Environmental Prediction–Department of Energy (NCEP–DOE) Reanalysis 2 (R2; Kanamitsu et al. 2002). All these atmospheric data are monthly averages with a 2.5° × 2.5° resolution.

Vertical wind shear is taken as the difference between the 200- and 850-hPa zonal winds. We use the same method as Colbert and Soden (2012) to define the steering flow for TCs, which is $0.25\mathbf{V}_{850\,\mathrm{hPa}} + 0.5\mathbf{V}_{500\,\mathrm{hPa}} + 0.25\mathbf{V}_{200\,\mathrm{hPa}}$ based on winds at 850, 500, and 200 hPa ($\mathbf{V}_{850\,\mathrm{hPa}}$, $\mathbf{V}_{500\,\mathrm{hPa}}$, and $\mathbf{V}_{200\,\mathrm{hPa}}$).

The HWG conducted the interannual experiments (1982–2009) with five different models. They are the FSU model (Cocke and LaRow 2000), the GFDL model (Zhao et al. 2009), the National Aeronautics and Space Administration (NASA) Goddard Institute for Space Studies (GISS) model E2 (Schmidt et al. 2014), the NASA Goddard Space Flight Center (GSFC) Earth Observing System Model, version 5 (GEOS-5; Rienecker et al. 2008; Molod et al. 2012), and the NCEP Global Forecast System (GFS) model (Buizza et al. 2005). Wang et al. (2014) and Walsh et al. (2015) provided more details about these models in terms of resolution, number of ensemble members, and different TC tracking schemes used by each modeling group. For the number of ensemble runs and model data resolutions, as well as the TC tracking algorithms for the five models, refer to Table 1 (also Table 1 in Wang et al. 2014). The sensitivity of the model TC activity to the different tracking algorithms in the HWG simulations has been discussed by Horn et al. (2014). They demonstrated that there are moderate agreements in

both TC geneses and TC tracks using different tracking schemes. However, some models (e.g., GFS) show better agreement across different tracking methods than others (e.g., GISS). This indicates a source of uncertainty in the analysis of TC activity as a result of different tracking schemes used by different modeling groups.

The annual total number of TCs and the spatial distribution of TC track density and origin depict the TC activity. Similar to Wang et al. (2014), this work adopts the following strategy for the analysis of TC track density and origin. Nondeveloping tropical depressions are excluded from the RSMC dataset. The TC origin in both the observation and model simulations is examined from the equator to 41°N and from 100°E to 180°, while the scope of TC track density is not defined in a specific region as long as the TC originates inside the defined region. The methodologies used to derive TC track density and define a TC origin are same as those in Wang et al. (2014). Briefly, the TC track density is the number of TCs passing through a 5° × 5° box during an entire hurricane season. The TC origin is the first location detected by the TC tracking schemes. For visualization, the TC origin data are gridded by a 5° × 5° (longitude × latitude) box.

The analysis focuses on the peak season of WNP TCs from July to October (JASO). Composites of both SST and atmospheric anomalies, including rainfall, 200–850-hPa wind shear, relative humidity, and tropospheric steering flow, are compared with each other between the three types of ENSO. The statistical significance of the analysis is determined by the Monte Carlo technique (e.g., von Storch and Zwiers 1999). This is done by first generating 500 new sets of data that are the same size as the original data by resampling the original data using random orders in time. Then the same analysis is repeated with these new datasets to create a pool of reference analysis statistics. If the result from the analysis with the original data falls into the top 5% rank in the reference tests, it is defined to be above the 95% significance level. The multimodel ensemble (MME) mean is the average of the five individual model ensemble means.

3. Variability of WNP TCs associated with ENSO in observations

The two El Niño categories are the same as those used by Wang et al. (2014), based on the definition by McPhaden et al. (2011). The La Niña years are selected according to NOAA/CPC (http://www.cpc.ncep.noaa.gov/products/analysis_monitoring/ensostuff/ensoyears.shtml). During the 28-yr period (1982–2009) there are five EP El Niño (1982, 1986, 1991, 1997, and 2006), five CP El Niño (1987, 1994, 2002, 2004, and 2009), and eight La Niña (1984, 1985, 1988, 1995, 1998, 1999, 2000, and 2007) years. The composites of JASO mean SST anomalies for the three types of ENSO shown on Fig. 1 display the representative characteristics (Ashok et al. 2007) of EP El Niño with warm SST anomalies in the equatorial eastern Pacific, CP El Niño with weak warm SST anomalies in the central Pacific, and La Niña with cold SST anomalies in the equatorial eastern and central Pacific.

Figure 2 shows the composite of the observed TC track density (upper row) and its anomaly (middle row) associated with the three ENSO types. Compared to the composites of the two types of El Niño (Figs. 2a,b), the TC track density in the La Niña years (Fig. 2c) has a smaller maximum, and its centroid is located farther westward and northward, which is consistent with previous studies (e.g., Wang and Chan 2002; Camargo and Sobel 2005; Kim et al. 2011). By contrast, the CP El Niño composite (Fig. 2b) of the TC tracks has an extension farther northeastward and westward than the EP El Niño (Fig. 2a).

Likewise, the anomaly composite of La Niña years (Fig. 2f) shows fewer TC tracks in the WNP than the El Niño composites (Figs. 2d,e). Both the composites of La Niña and CP El Niño show positive TC track density anomalies along the East Asia coast, indicating above-normal landfalling TCs. Landfalling TCs tend to be below normal during EP El Niño. The anomaly differences in TC track density between the EP and CP El Niño (Figs. 2d,e) clearly show a higher TC track density of the CP El Niño over the northwestern part of the WNP (positive anomalies) but a lower density over the southern part of the WNP (positive but weaker anomalies), especially from the eastern South China Sea (SCS) to the Philippines (negative anomalies). The composite anomalies in Fig. 2 (middle row) within the white contours are statistically significant above the 95% level estimated by the Monte Carlo test. The anomaly patterns are very similar to those in Kim et al. (2011), which contain a longer record (57 yr, 1950–2006).

Additionally, Fig. 2 (bottom row) also shows the locations of TC origins for each ENSO category. To be consistent with the sample size for both the EP and CP El Niño, the five La Niña events of 1985, 1988, 1998, 1999, and 2007 are selected based on the Niño-3.4 SST index as the coldest five years averaged from July to October. Compared to EP El Niño years (Fig. 2g), there is a distinct westward and northward shift of TC origins during La Niña (Fig. 2i) and to some extent during CP El Niño (Fig. 2h) events, with both ENSO types having more TC origins over the SCS. The total numbers of TC origins in the WNP domain (110°E – 180°, 0° – 41°N) are 127, 128, and 108 for the five EP El Niño, five CP El Niño, and five La Niña events, respectively. Because it is

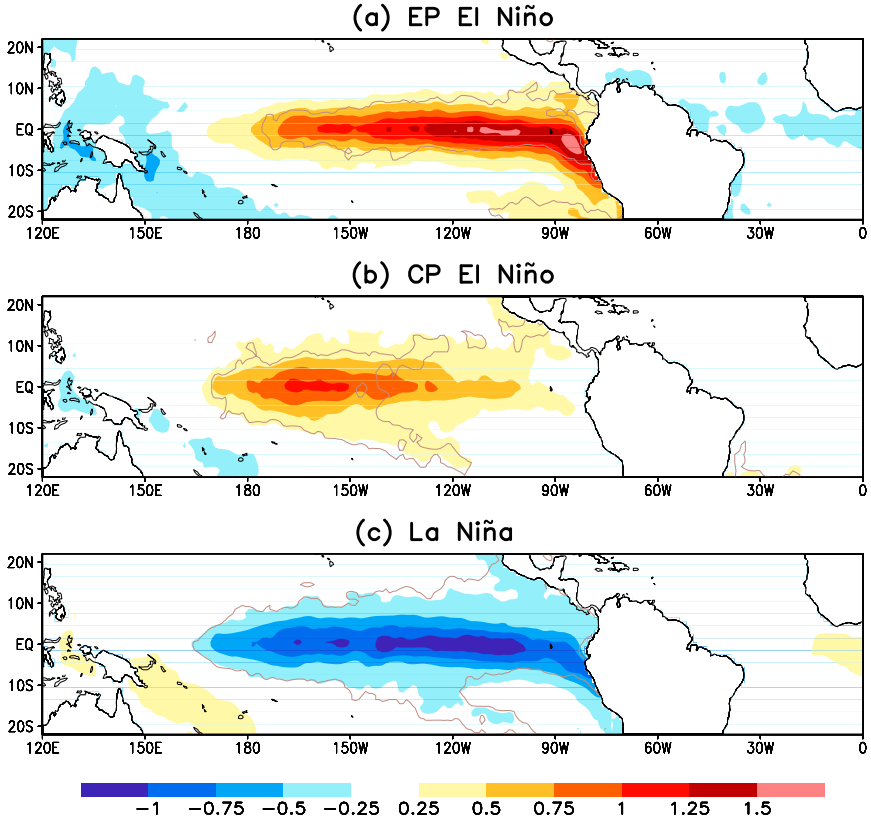

FIG. 1. Composites of JASO mean SST anomalies (K) for (a) EP El Niño (1982, 1986, 1991, 1997, and 2006); (b) CP El Niño (1987, 1994, 2002, 2004, and 2009); and (c) La Niña (1984, 1985, 1988, 1995, 1998, 1999, 2000, and 2007) during 1982–2009. The SST anomalies circled by the brown lines are above the 99% significance level estimated by the Monte Carlo test.

hard to discern the differences in numbers and locations of TC origins between the three ENSO categories, further analyses will be done in section 4c based on the zonal and meridional distributions of TC origins in different ENSO categories.

4. Assessment of variability in WNP TCs and its association with ENSO in GCMs

a. Annual number of TCs

The statistical characteristics of the interannual variation of the annual number of WNP TCs from 1982 to 2009 are displayed in Fig. 3 and Table 2. In Fig. 3, nearly 86% (24 out of 28 yr) of the observations fall into the range of the spreads of the five individual model ensemble means from the MME mean (gray shading), suggesting the possible predictability of the TC annual number during the peak TC season. The GFDL model has the highest mean numbers (33.8) of TCs, while the FSU model has the lowest numbers (15.8) of TCs among all models (Table 2). Overall, the MME mean result (25.4) is the closest to the observations (24.6) among all individual models, implying the benefit of performing an MME mean.

In addition to the differences in the mean annual number, the standard deviations show that the GISS and GFS models have the same value (3.6) and are the closest to observations (3.5). The standard deviations of the FSU model (2.3) and MME (2.7) are also close to observations. However, the standard deviations of the GFDL model (5.6) and the GSFC model (4.7) are larger than observations, suggesting higher annual TC number variations in the two models. Furthermore, the observations have a slightly declining trend with −1.4 TCs per decade, which is statistically significant at the 95% confidence level and consistent with Ho et al. (2004), who showed a decreasing TC track density over the East China Sea and the Philippine Sea. The models that have a similar trend are the GFDL [−0.9 TC per decade, similar to Zhao et al. (2009), with −0.7 TC per decade over the simulated period of 1981–2005] and GISS (−0.7) models, although

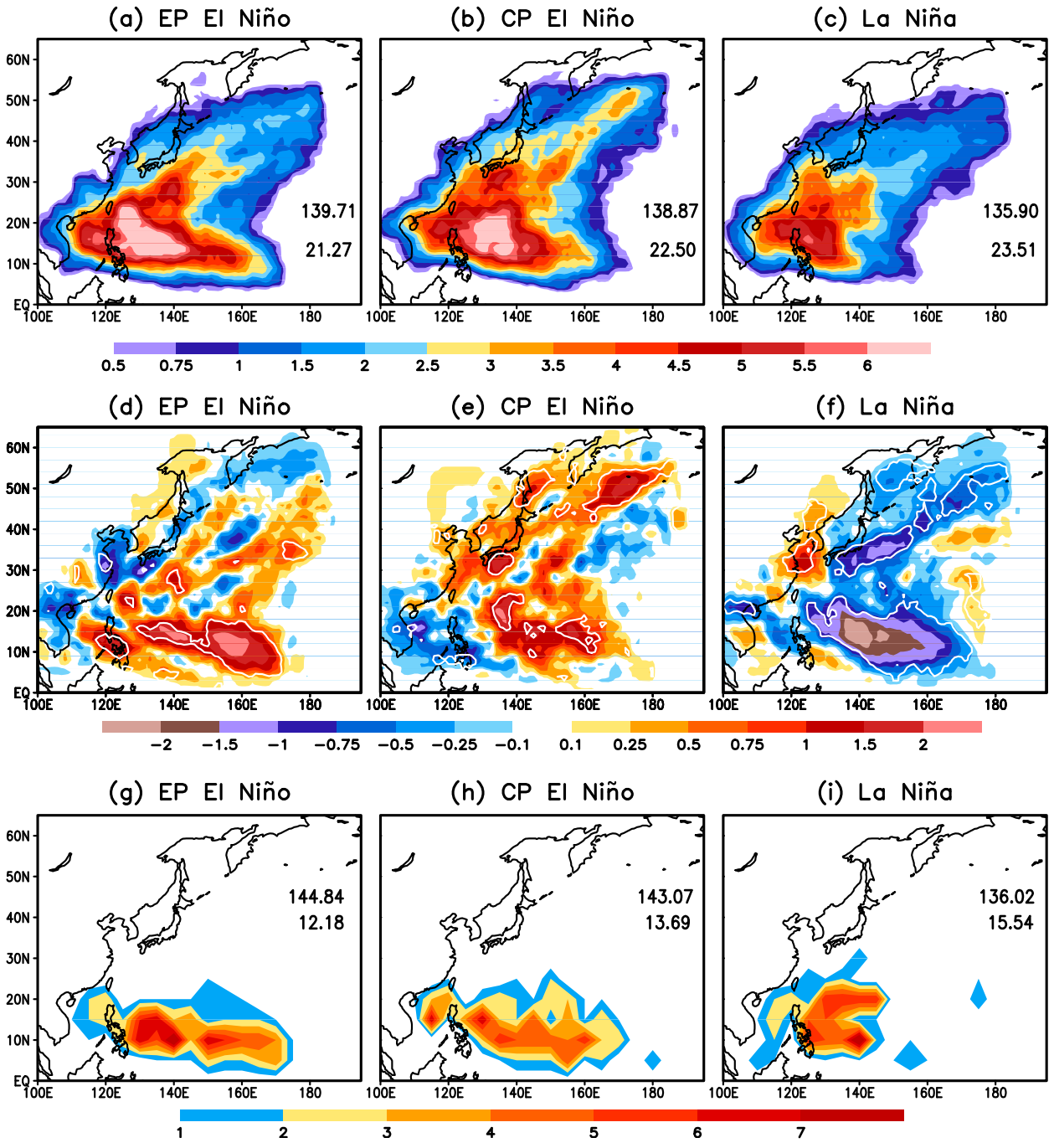

FIG. 2. Composites of (top) TC track density, (middle) track density anomaly, and (bottom) TC origins for (a),(d),(g) EP El Niño; (b),(e),(h) CP El Niño; and (c),(f),(i) La Niña years in the observations. The composites are for all the cases, except for (i) the TC origins in La Niña years, in which only the strongest five events are used in order to have the same sample size for comparison. The light white contours in (d)–(f) represent the 95% significance level estimated by the Monte Carlo test. The longitude (°E) and latitude (°N) of the centroids of TC track density and TC origins are listed on each panel.

most of the model trends are weaker than the observations, whereas the GSFC (1.6) and GFS (0.9) models have an unrealistic upward trend. The FSU model (0.0) has no trend during the 28 yr. None of the trends in the models are statistically significant, except the GSFC model at the 90% confidence level.

In terms of anomaly correlation (AC; Table 2), the individual ensemble mean of the GISS model has the

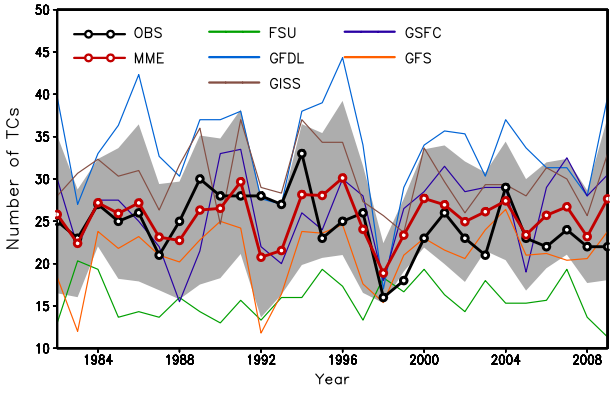

FIG. 3. Time series of annual number of WNP TCs from 1982 to 2009 for observations (OBS; black with open circles) and MME mean (thick red line with open circles), as well as individual model ensemble means (thin lines: FSU green, GFDL blue, GISS brown, GSFC purple, and GFS orange). Gray shading denotes the spread of the five individual model ensemble means around the MME mean, measured by ±1 standard deviation of 5 individual model ensemble means from the MME mean.

TABLE 2. List of TC statistics for observations, MME mean, and individual model ensemble means, including 28-yr (1982–2009) long-term mean annual number of WNP TCs, standard deviation, linear trend (increase of TCs per decade), AC between observations and model-simulated interannual TC anomalies, and RMSE. The trend and the ACs in bold are above the 95% significance level.

Model	Mean	Std dev	Trend	AC	RMSE
Observation	24.6	3.5	**−1.4**		
MME	25.4	2.7	0.2	**0.43**	3.48
FSU	15.8	2.3	0.0	−0.22	9.96
GFDL	33.8	5.6	−0.9	**0.50**	10.38
GISS	30.1	3.6	−0.7	**0.51**	6.55
GSFC	26.3	4.7	1.6	0.16	5.65
GFS	21.0	3.6	0.9	0.24	5.65

highest value (0.51), followed by the GFDL model (0.50), and the MME (0.43), all statistically significant at the 95% confidence level (ACs for the other models are not significant). The results indicate that 25% of the observed interannual TC variance is captured by both the GISS and GFDL models and 18% by the MME (von Storch and Zwiers 1999). We note that ACs in Table 2 are lower than ACs for the Atlantic (Wang et al. 2014), which is consistent with previous work (e.g., Zhao et al. 2009; Chen and Lin 2013; Shaevitz et al. 2014) and implies that TC predictability may be higher in the Atlantic than in the WNP. Similarly, the ACs obtained by Shaevitz et al. (2014) in WNP are −0.25 for the FSU model, 0.24 for the GSFC model, and 0.55 for the GFDL model. The one exception is the GISS model with an AC of 0.21, which is much lower than the AC value of 0.51 seen in Table 2. The remarkable discrepancy may originate primarily from different detection periods of annual TC number. In this study, the period is from June to November, while it is for the whole year in Shaevitz et al. (2014). Additionally, the MME has the smallest root-mean-square error (RMSE), while the GFDL and FSU models have relatively larger RMSEs. Zhao et al. (2009) pointed out that the convective entrainment rate designed in the GFDL model is high and unrealistic for the WNP but suitable for the North Atlantic. That may be a reason for the overestimated annual mean numbers of TCs, the standard deviation, and the large RMSE in the GFDL model (Table 2).

b. *Track densities and origins of TCs*

The spatial distributions of the 28-yr mean TC track densities and total TC origins are shown on Fig. 4 for both observations and simulations. Unlike the observed TC track density (Fig. 4a), the TC track densities in the models are confined to south of 41°N (Figs. 4c–h). This could be an artifact of either the tracking schemes or sample errors in the observations or both, as the best-track dataset typically does not have a specific extratropical quantitative cutoff for stopping the tracking of TCs. A sensitivity study of TC tracks to tracking schemes by Horn et al. (2014, their Figs. 4h,i) illustrates that in the GISS model, the WNP TC tracks based on Camargo and Zebiak (2002) have a farther northward extension than those based on the Zhao et al. (2009) scheme. Overall, however, the distributions of TC track densities in the five models and MME are similar to the observations with the center of high track density over the subtropics. The maximum TC track densities in the GFDL, GSFC, and GFS simulations (Figs. 4d,f,g) are comparable to the observations, while the maxima in the FSU and GISS simulations and MME (Figs. 4c,e,h) are smaller than observations. Only the locations of the maximum centers in the GFDL and FSU models coincide with that of the observations, and those in the other three models and MME are biased eastward (and southward in GSFC). Among the five models, the GFDL model has the best performance in simulating the TC track density, which is closest to the observations in terms of both the spatial distribution and magnitude.

The TC origins in the observations (Fig. 4b) are characterized by two regions of large concentrations: one located in the eastern SCS and the other from the east of the Philippine islands to the west of 160°E, both between 5° and 20°N. The FSU, GFDL, and GSFC models exhibit distributions somewhat similar to the observations (Figs. 4i,j,l), though the FSU distribution is too narrow meridionally. However, the GISS model shows some unrealistic origins over southern China and near the date line, leading to the same bias in the MME mean (Fig. 4n). TC origins in the GFS model have a strong eastward shift compared with the observations.

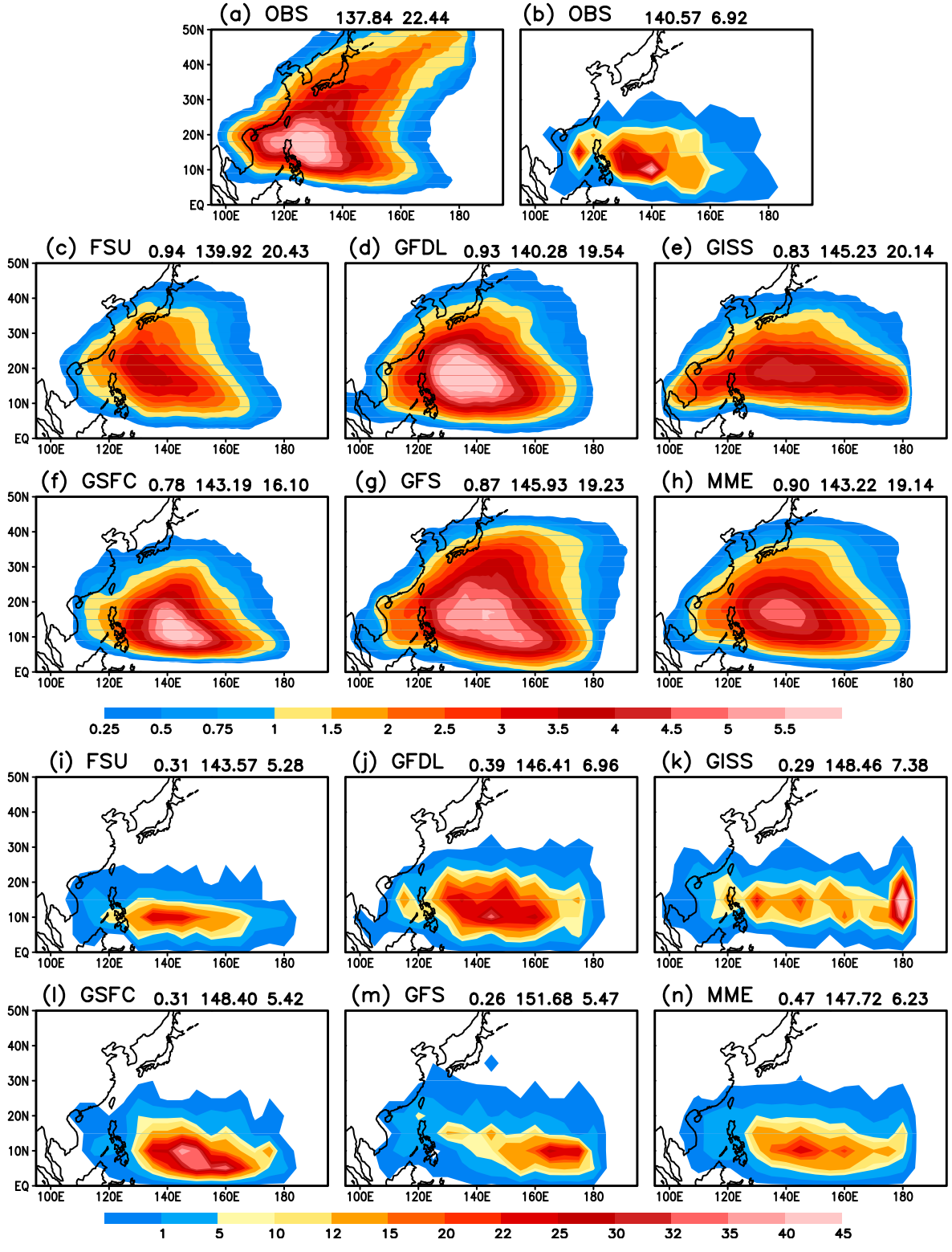

FIG. 4. Climatology of track density for (a) observations, (c)–(g) individual model ensemble means, and (h) MME mean and 28-yr total TC origins gridded as in Fig. 2, for (b) observations, (i)–(m) one ensemble member of each model, and (n) MME total from one member of each model. The longitude (°E) and latitude (°N) of the centroids of the observed TC track density and TC origins are listed at the top of (a) and (b), respectively. The pattern correlation between the (c)–(n) model simulated and the (a),(b) observed and the corresponding centroids in the models are listed at the tops of (c)–(n).

Overall, for TC origins, the GFDL model (Fig. 4j) has the distribution closest to the observations, and the MME mean also shows a good representation, with the exception of the date line region (Fig. 4n). Consistently, both the GFDL model and the MME mean have relatively high pattern correlations with observations for both the TC track density and TC origins. Their corresponding centroids are also among the closest to the observations.

To further compare the magnitude and spatial distribution between the simulations and observations, TC origins are summed separately along longitudinal and latitudinal circles after undergoing a smoothing process similar to that for deriving track density described by Wang et al. (2014). The TC origins summed in the 5° × 5° boxes are smoothed with eight surrounding grid points with a weighting coefficient of ½ for the central grid point and 1/16 for the surrounding grid points. Additionally, the values are further smoothed using a 3-point running mean along longitude or latitude (as shown in Figs. 5, 8, and 9). For the climatological TC origins summed meridionally from the equator to 41°N (Fig. 5, left column), the observed TC origins (black curve) exhibit a high-value zone between 130° and 155°E, and three low-value zones in the western and eastern ends of the WNP and near 120°E (Philippines). The FSU, GFDL, and GSFC models perform reasonably well with similar characteristics and are also highly correlated with observations (0.79, 0.68, and 0.58). The correlation for the MME is 0.54. Compared to the observations, the FSU model underestimates TC origins between 110° and 160°E, while the GFDL model overestimates TC origins east of 135°E. Both the GFDL and GISS models simulate well the peak of TC origins around 115°E. The GISS model slightly underestimates the number of TC origins to the west of 160°E and largely overestimates it at the date line, which is related to the model systematic error seen in Fig. 4k. The GFS model shows large biases in both the observed high- and low-value zones (distribution shifted eastward). The GSFC model also has a similar shift, although not as pronounced.

For the climatological TC origins summed longitudinally from 100°E to 180° (Fig. 5, right column), the distribution of the observed TC origins (black curve) peaks between 8° and 17°N. The GFDL and GISS models and the MME show similar distributions with latitude. Compared to the observations, the FSU, GSFC, and GFS models show peaks shifted southward with fewer TC formations to the north. Based on the correlations between model simulations and observations shown on Fig. 5, the models can capture better the distribution of TC origins along latitude (Fig. 5, right column) than the distribution along longitude (Fig. 5, left column).

c. Association with ENSO

Similar to the observations (Fig. 2, top), the ENSO composites of track density for individual model ensemble means and the MME means are shown on Fig. 6. Although there are biases in the spatial distribution of climatology in each model revealed in Fig. 4, the composites for the three ENSO types consistently exhibit higher TC track densities during EP and CP El Niño (Fig. 6, left and middle) and lower track densities during La Niña (Fig. 6, right), except for the FSU and GISS models. However, the contrast between EP and CP El Niño track density composites in the northeast part of the WNP (Figs. 2a,b) cannot be seen in all models' simulations. The GFDL model has the best performance in simulating the spatial distribution of TC density for La Niña (Fig. 6, second row, right panel), indicated by a pattern correlation of 0.89.

The corresponding composites for track density anomaly with respect to model climatology are displayed in Fig. 7. Most of the models except for the FSU model (and GISS model, to some extent) show above-normal track densities across large parts of the WNP during the two types of El Niño (Fig. 7, left and middle) and below normal track densities during La Niña (Fig. 7, right). Furthermore, the FSU, GISS, and GFS models, and the MME are all able to capture the characteristics of more landfalling TCs along the coast of southeastern China during La Niña (Fig. 7, right) and fewer landfalling TCs during EP El Niño (Fig. 7, left). Although there are differences between the EP and CP El Niño composites (Fig. 7, left and middle), none of the model simulations resembles the observations (Figs. 2d,e), suggesting a challenge for modeling the distinguishing impacts of two types of El Niño on TC track density.

Figures 8 and 9 show the TC origin composites for the three ENSO types as a function of longitude and latitude, respectively, for each model ensemble mean and MME mean together with the observations (black curve). For a fair comparison with five EP and CP El Niño events, the composite for La Niña is based on the strongest five episodes aforementioned. It is clear that the peaks in the composite of the observed TC origins for La Niña have more westward locations and slightly higher values than those in the EP and CP El Niño composites (as shown by black curves in Fig. 8; also seen in Figs. 2g,h,i), which cannot be captured completely by any models. The main difference between the EP and CP El Niño composites is the relatively high TC formations to the west of 120°E in the CP El Niño with 3.4 per CP El Niño year and 2.2 per

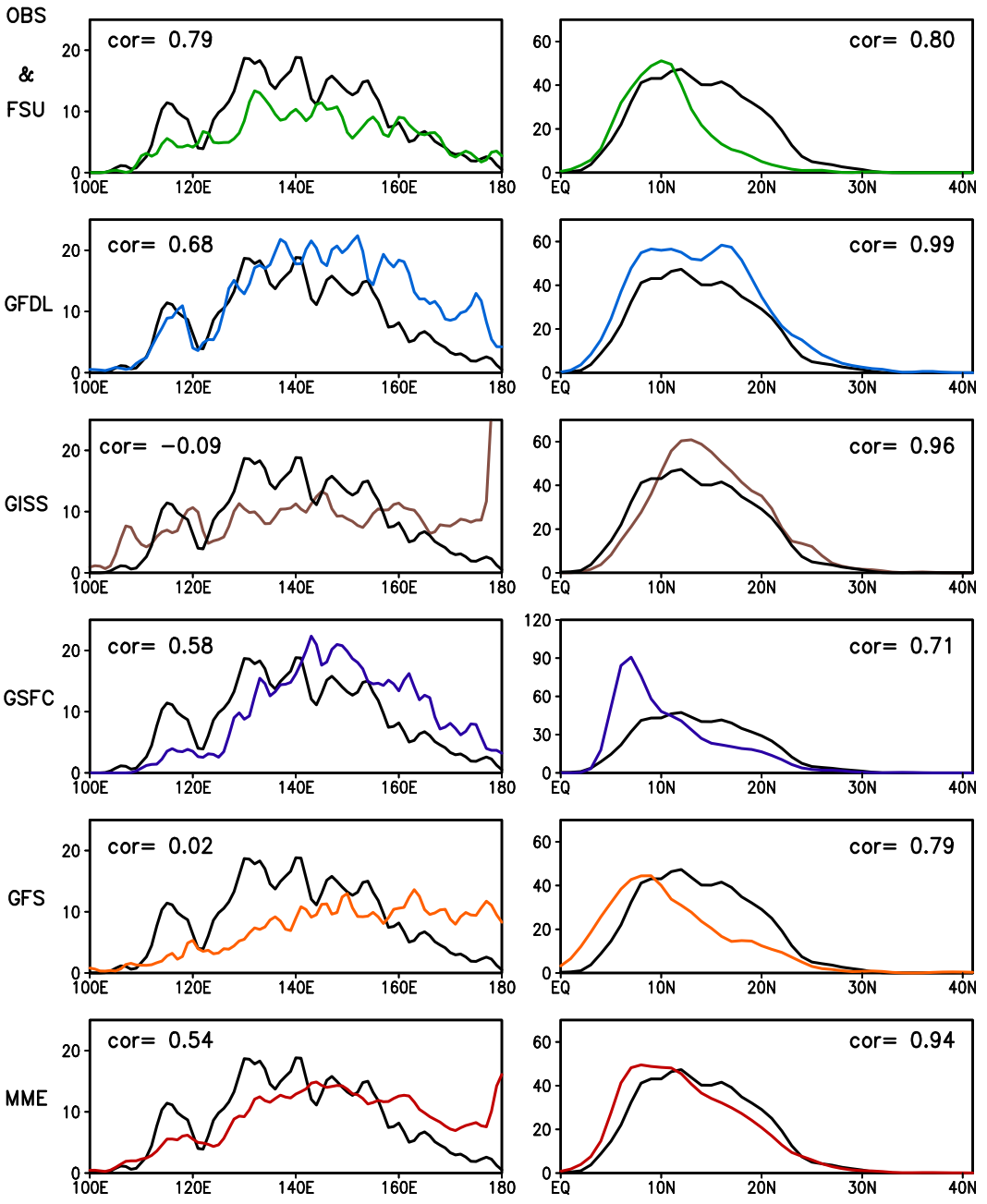

FIG. 5. Climatology of 28-yr total TC origins (left) summed from the equator to 41°N as a function of longitude and (right) summed from 100°E to 180° as a function of latitude. The black lines are for observations and colored lines for model results. The values are smoothed with the method described in section 4b. The Pearson correlation (cor) of climatological TC origins between the models (color lines) and observations (black line) is listed for each panel.

EP El Niño year. The FSU and GFDL models can distinguish the aforementioned main discrepancy between the two types of El Niño. For La Niña (right column of Fig. 8), the FSU, GFDL, and GSFC models simulate the peaks in the western Pacific between 110° and 120°E better than the other models. Although there are biases in simulating the variations in TC origins with longitude in the three ENSO categories, most models can better simulate the variability of TC origins with longitude in both the EP and CP El Niño than in La Niña, as indicated by the Pearson correlation coefficients.

Figure 9 indicates there is a peak near 10°N in the observed TC origins in both El Niño categories, though slightly weaker in CP El Niño. In the La Niña, the largest

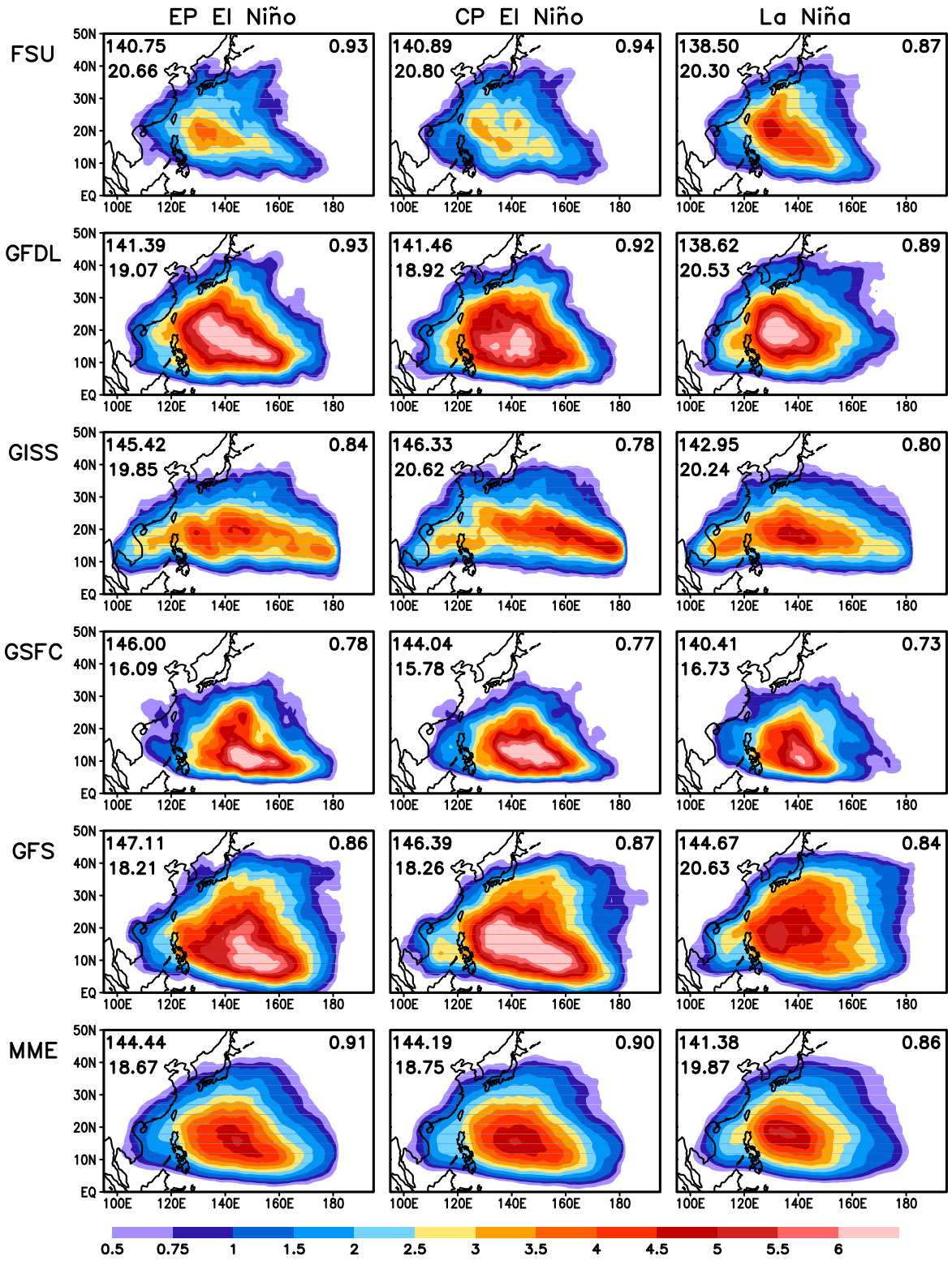

FIG. 6. Composites of track density during (left) EP El Niño, (center) CP El Niño, and (right) La Niña for (top five rows) five individual model ensemble means and (bottom row) MME mean. The longitude (°E) and latitude (°N) of the centroid of the simulated TC track density are listed on the upper-left side, and the pattern correlation with corresponding observations (Figs. 2a–c) on the upper right.

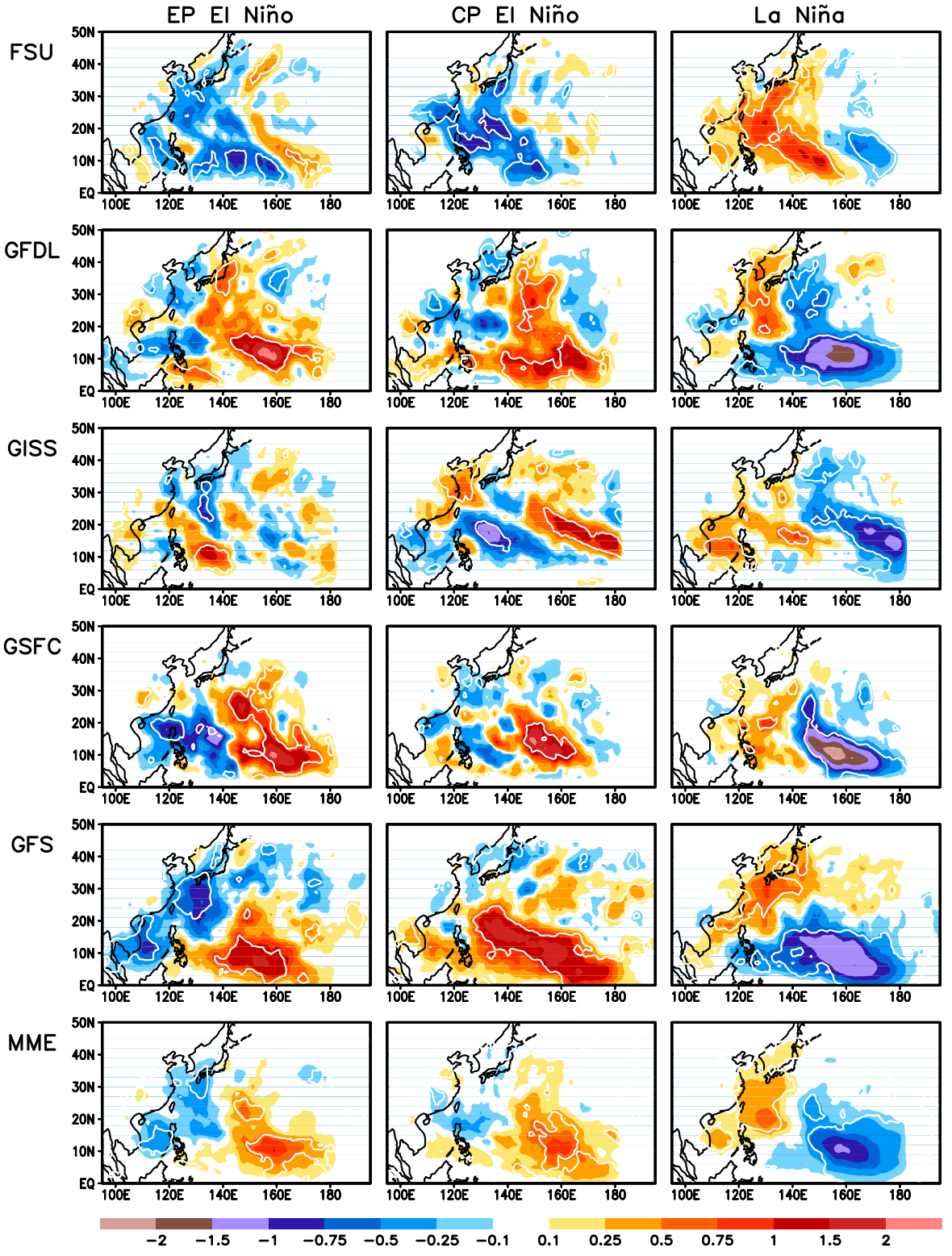

FIG. 7. As in Fig. 6, but for composites of TC track density anomaly with respect to model climatology. The light white contours represent the 95% significance level.

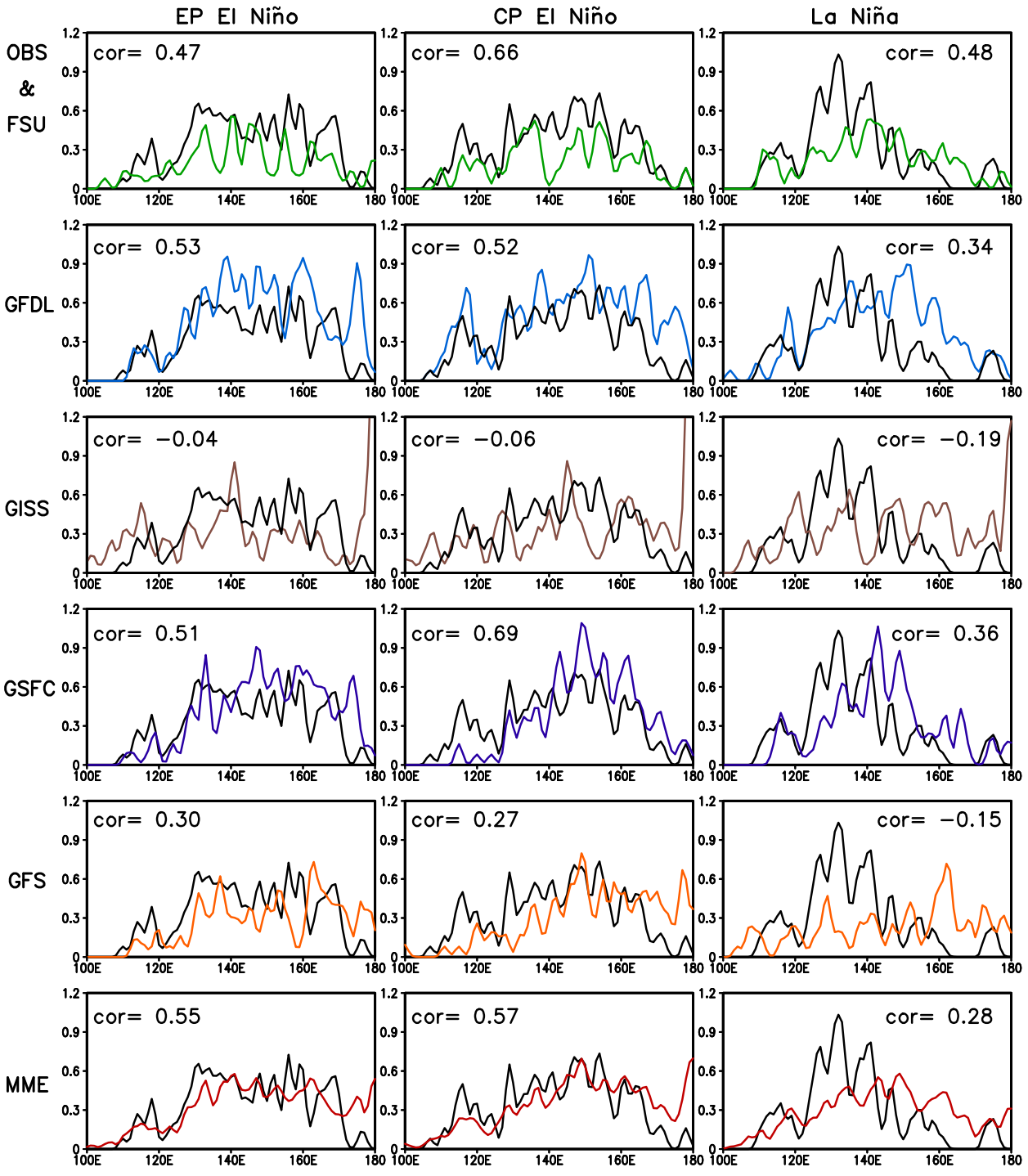

FIG. 8. As in the left panels of Fig. 5, but for five (left) EP El Niño, (center) CP El Niño, and (right) La Niña years.

peak is found near 20°N with a secondary one near 10°N. Most of the models and the MME mean reproduce the distribution of TC origins with latitudes in EP El Niño, except for the GSFC model (and GFS to some extent). For CP El Niño, the FSU, GFDL, and GISS models, as well as the MME mean, capture the changes in TC origins with latitude, but the GSFC and GFS models have apparent discrepancies. The simulations of the distribution of the TC origins in La Niña seem difficult for the GCMs, with the exception of the GFDL and GISS models. Overall, the GFDL and GISS models and the MME capture the different characteristics of the TC origins

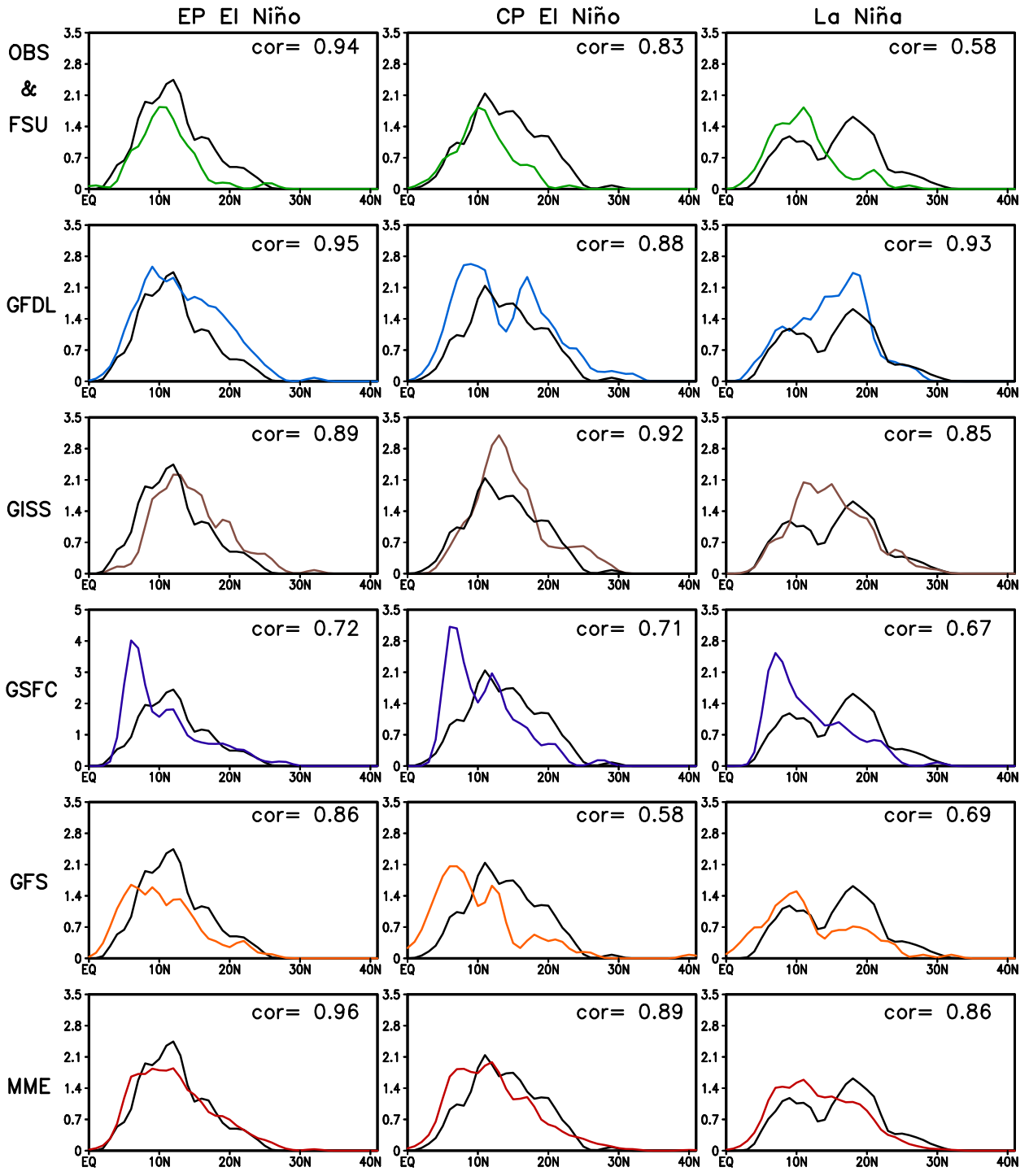

FIG. 9. As in the right panels of Fig. 5, but for five (left) EP El Niño, (center) CP El Niño, and (right) La Niña years.

among the three ENSO categories, which is also evident by the correlation coefficients.

5. Possible explanations for model biases

The changes in both the mean and variability of TCs are closely related to the changes in thermodynamic states and large-scale circulation patterns, which are often employed to detect the causes of biases in model simulations (e.g., Zhao et al. 2009; Wang et al. 2014; Shaevitz et al. 2014; Walsh et al. 2015) and differentiate the discrepancies of TC behaviors among different ENSO categories (e.g., Chen and Tam 2010; Kim et al.

2011; Hong et al. 2011). The key atmospheric conditions favorable for TC formation are ascending motions over warm SST, moistened midtroposphere, and weak vertical wind shear (e.g., Camargo et al. 2007a; Kim et al. 2011). The following analyses focus on these atmospheric factors in order to examine the possible causes of the biases of TC activity in the GCM simulations.

The JASO mean climatology of the observed 200–850-hPa vertical wind shear and the mean biases of the vertical wind shear and climatology of TC origin for each model ensemble mean and the MME are shown in Fig. 10. For the observed climatology of vertical shear (Fig. 10a), the region within a small magnitude of negative vertical shear over the northeast of the Philippines coincides with the region of high TC track density and dense TC origins in the observations (Figs. 4a,b).

In the model simulations, there seems to be a correspondence between the biases in the vertical wind shear (Figs. 10b–g) and the TC origins (Figs. 10h–m), especially over the low-latitude ocean between the equator and 20°N. For example, the negative biases of vertical shear in all five models and the MME located east of 160°E (Figs. 10b–g) relative to the observed positive vertical shear in the same region (Fig. 10a) indicate weakened vertical shear in the simulations. Consequently, a bias of enhanced TC origins is found in the same region in all the simulations (Fig. 10h–m). On the other hand, the negative biases of vertical wind shear in the MME and all models except the GFS over the region from the south of Taiwan to the northern SCS have the same sign as the observed negative vertical wind shear in the same region (Fig. 10a) and thus indicate an enhanced vertical shear in the simulations. As a result, there is a bias of decreased TC origins in all five models and the MME simulations distributed in the same region from the south of Taiwan to the northern SCS (Figs. 10h–m).

Figure 11 displays the composites of JASO mean vertical wind shear anomalies associated with the three ENSO categories for the observations (Figs. 11a–c) and MME (Figs. 11d–f), respectively. To some extent, the model responses to different ENSO phases are consistent with the observations. Associated with the EP El Niño (Figs. 11a,d), the negative vertical wind shear anomalies in the central and eastern parts of the WNP, which favor TC activity in the southeast part of the WNP (Figs. 2d, 7), are found in both the observations and MME. The distributions of opposite anomalies associated with La Niña (Figs. 11c,f) are also evident in both the observations and MME. Likewise, they are associated with reduced TC activity in the southeast WNP (Figs. 2f, 7). The MME fails to capture the fine structure of wind shear anomalies over eastern China during CP El Niño (Figs. 11b,e). However, as with the EP El Niño, increased TC activity associated with reduced wind shear in the southeast part of the WNP is found for both MME and the observations (Figs. 2e, 7). In general, for the three ENSO categories, the models simulate the wind shear anomalies better in the low latitudes (0°–20°N) than in the higher latitudes (20°–40°N). The simulations in the low latitudes are better to the east of 120°E than to the west.

It is well known that there are other factors also affecting TC activity, such as SST (Graham et al. 1987), midlevel moisture (Gray 1979; Camargo et al. 2007a), and tropical deep convection (Kim et al. 2011). The tropical deep convection is known to be related to SST heating and sufficient midlevel moisture, which in turn provides a heating source for the atmosphere. Therefore, the different locations of SST anomalies in the ENSO categories may lead to changes in deep convection over the tropical Pacific and, thus, changes in the atmospheric response.

In the tropics, deep convection and the associated heating of the atmosphere can be well represented by the distribution of tropical precipitation (e.g., Wang et al. 2012, 2014). Figure 12 shows the composites of JASO mean precipitation anomalies in each ENSO category for both observations and the MME. Consistent with the observations, the MME shows above-normal precipitation in the eastern and central Pacific during EP El Niño (Figs. 12a,d) and below-normal precipitation during La Niña (Figs. 12c,f). Associated with CP El Niño, there are similar anomalies in precipitation but with a smaller magnitude and shifted westward as compared with EP El Niño. This kind of contrast of the deep convection (precipitation) associated with EP and CP El Niño has been noted in previous studies, such as Hu et al. (2012). Therefore, it is evident that the GCMs simulate well the precipitation anomalies over the tropical Pacific associated with the three ENSO categories. However, some deficiencies exist in the simulations; for example, the anomalies are much weaker over the Maritime Continent and between 160°E and 180° for all ENSO categories. These deficiencies may be responsible for the biases of TC formations in the MME, in which there are negative (positive) TC origin biases over the southeastern (northwestern) part of the WNP during the two types of El Niño events (Fig. 12g,h), while the opposite is true during La Niña events (Fig. 12i).

Midlevel moisture is also a key factor affecting both TC climatology (Cheung 2004) and ENSO-induced variability (e.g., Camargo et al. 2007a). Figure 13 shows the observed and simulated (MME) JASO mean climatology of 500-hPa relative humidity and the

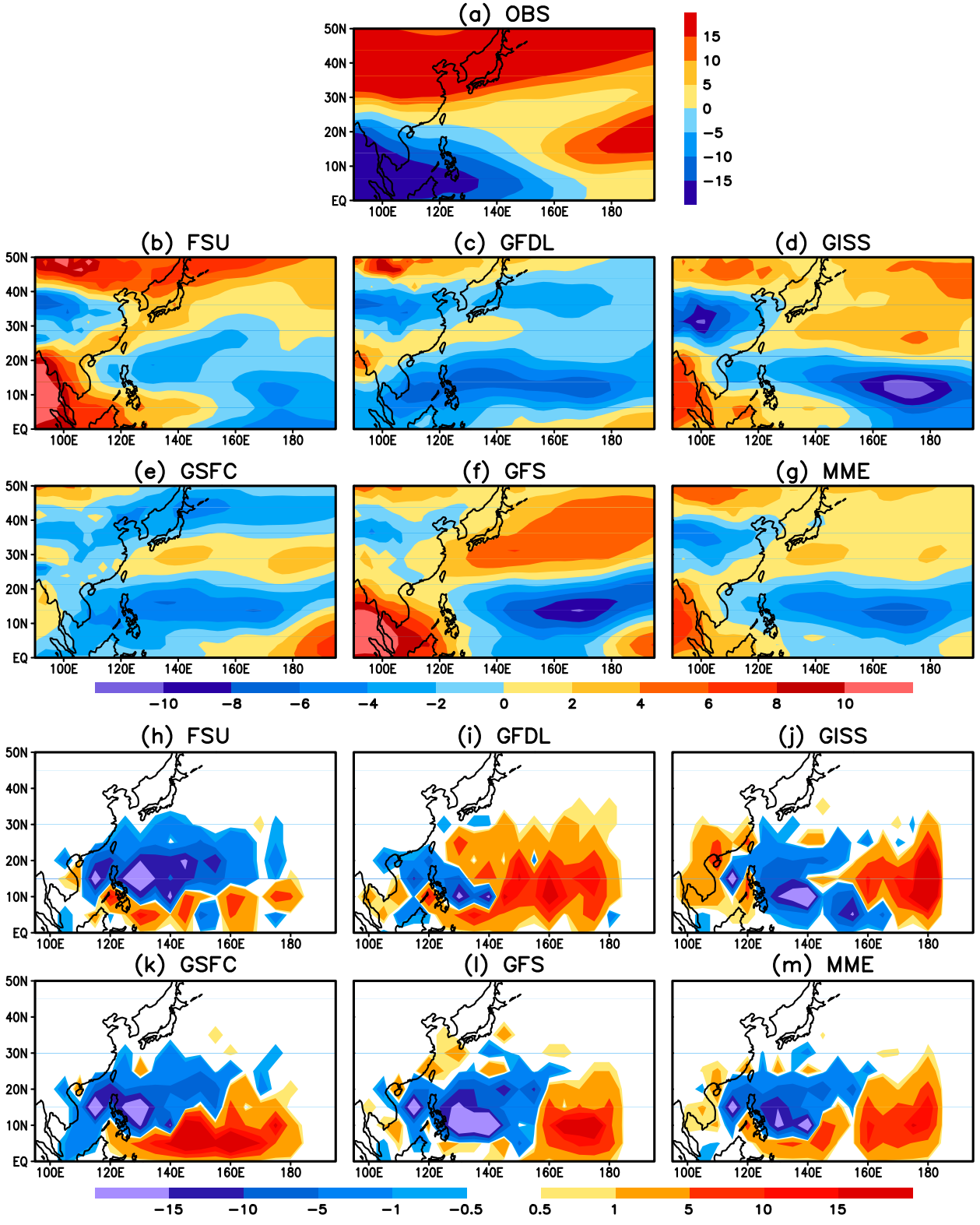

FIG. 10. (a) Observed JASO climatology of vertical shear of zonal wind ($m\,s^{-1}$) between 200 and 850 hPa and mean bias in the (b) FSU, (c) GFDL, (d) GISS, (e) GSFC, and (f) GFS models, as well as in (g) the MME; (h)–(m) the corresponding mean bias of TC origin.

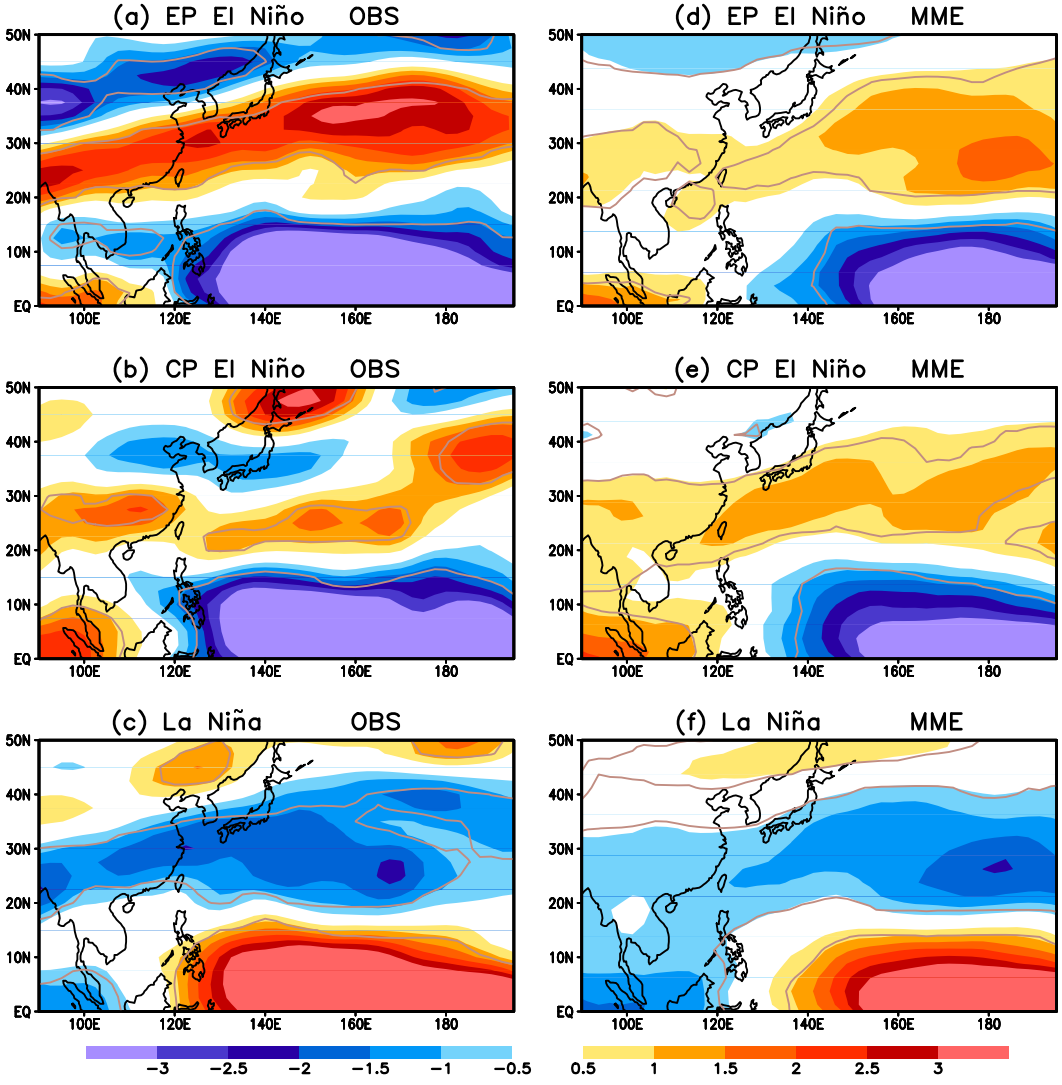

FIG. 11. Composites of JASO mean vertical wind shear anomalies ($m\,s^{-1}$) for (a),(d) EP El Niño; (b),(e) CP El Niño; and (c),(f) La Niña during 1982–2009 in (a)–(c) observations and (d)–(f) the MME mean. The light gray contours represent the 90% significance level.

composites of corresponding anomalies for each type of ENSO. As compared with the observations (Fig. 13a), the moistened atmosphere south of 20°N and east of 130°E in the MME (Fig. 13b) may be related to the overestimated TC track density expanding eastward toward the date line, which is not found in the observations (Figs. 4a,h). In contrast, the drier atmosphere over the region from the Sea of Japan stretching southward to Taiwan likely leads to a locally sparser TC track density in MME than in the observations (Figs. 4a, h or Fig. 10m).

In general, the ENSO-related humidity anomalies in the MME mean (Fig. 13, right) are weak over the southeastern part of the WNP and strong over the northwestern part of the WNP as compared to the observations (Fig. 13, left). For instance, the composites of the relative humidity anomalies for the EP and CP El Niño show lower moisture over the central and eastern parts of the WNP in the MME (Figs. 13f,g) than in the observations (Figs. 13b,c). These coincide with the lower TC track density over the central and eastern parts of the WNP in the MME (Fig. 7, two bottom-left panels) than in the observations (Figs. 2d,e). Associated with La Niña, the positive anomalies over the central and western parts of the WNP are farther east in the MME (Fig. 13h) than in the observations (Fig. 13d). The positive anomalies over the southwest part of the WNP are weaker in intensity and smaller in extent than in the observations. These biases may be related to the positive TC track density anomalies in the MME

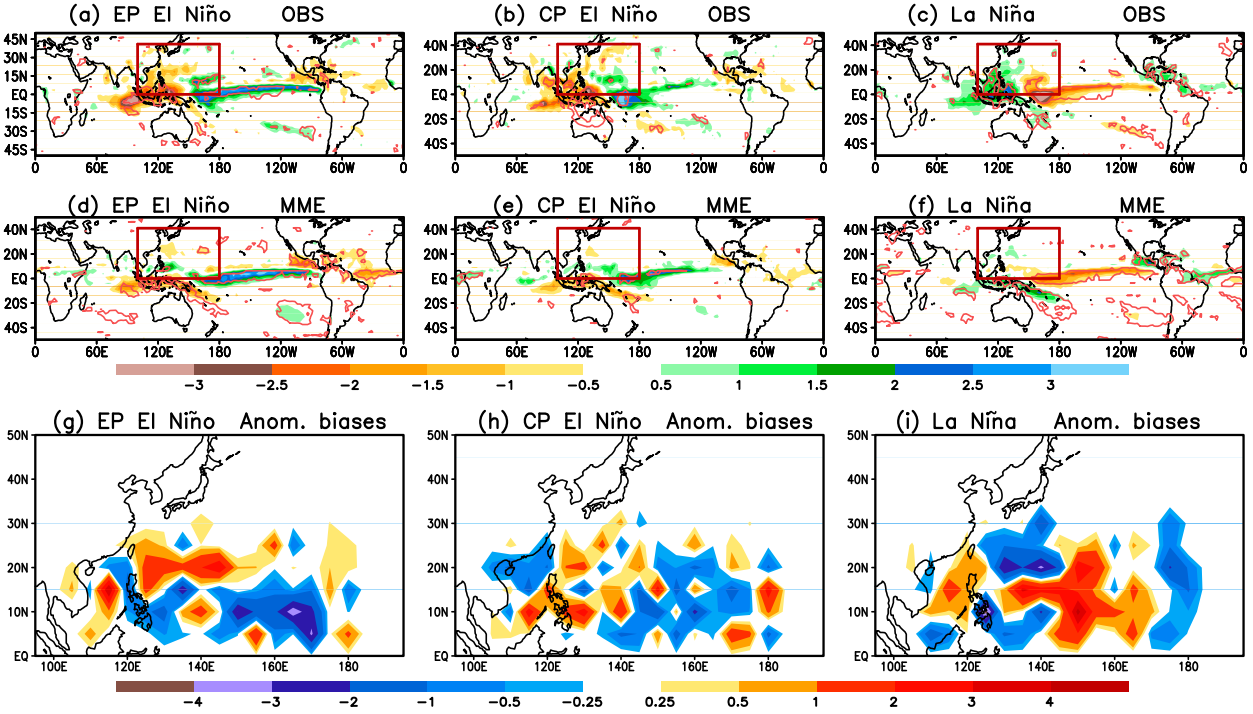

FIG. 12. (top),(middle) Composites of JASO mean precipitation anomalies (mm day^{-1}) and (bottom) the biases of composites of anomaly TC origin for (a),(d),(g) EP El Niño; (b),(e),(h) CP El Niño; and (c),(f),(i) La Niña during 1982–2009 for (a)–(c) observations, (d)–(f) the MME mean, and (g)–(i) the biases of TC origins. The composites are based on the five EP El Niño, five CP El Niño, and five strongest La Niña years. The anomalies circled by the light red lines in (a)–(f) are above the 99% significance level. The red box in (a)–(f) denotes the NWP region.

shifting toward the east of the coast off east Asia and the sparse TC track density over the SCS (Fig. 7, bottom-right panel), as compared with the observations (Fig. 2f).

Changes in TC tracks between El Niño and La Niña years are largely due to changes in steering flow (Colbert and Soden 2012). The anomaly composites of the JASO steering flow for each ENSO category are shown in Fig. 14 for both observations and the MME, together with the corresponding TC track density anomalies. In the observations, the positive (negative) anomalies of TC track density generally match the southerly (northerly) steering flow. Off the coast of southeastern Asia, more (fewer) landfalling TCs are consistent with onshore (offshore) winds. In both EP and CP El Niño composites (Figs. 14a,b), the positive anomalies of TC track density match the southerlies, which cover most parts of the WNP except for some regions, such as the SCS. The opposite occurs in the composite of La Niña (Fig. 14c). Between EP and CP El Niño (Figs. 14a,b), the differences in the deep-layer steering flow can also be seen, for example, in the northerly winds over the coast of East Asia in EP El Niño and the southeasterly winds in CP El Niño. Consequently, there are fewer landfalling TCs over the coast of East Asia in EP El Niño (Fig. 14a) and more in CP El Niño (Fig. 14b).

In the MME (Figs. 14d,e), for both the EP and CP El Niño composites there are southerlies shifting southeastward compared with the observations (Figs. 14a,b). The anomalies of TC track density in both the EP and CP El Niño thus locate farther southeast in the MME than in the observations. There are offshore winds over the coast of East Asia in CP El Niño (Fig. 14e) but onshore winds in the observations (Fig. 14b), which leads to the MME bias of less TC track density over the coast of East Asia than in the observations. Concerning the deep-layer steering flow in La Niña years, there are also biases in the MME (Fig. 14f), with easterly winds near the central coast of China between 120° and 140°E but northerlies over the same region in the observations (Fig. 14c). This is consistent with the positive TC track density in the MME and the negative anomalies in the observations (Figs. 14c,f). Overall, the less southerly but more zonal steering flow in the MME seems associated with weaker TC track density anomalies.

6. Summary and conclusions

Based on the output data of the HWG experiments, the multimodel performance in simulating the variability of TCs in the WNP and its association with ENSO are

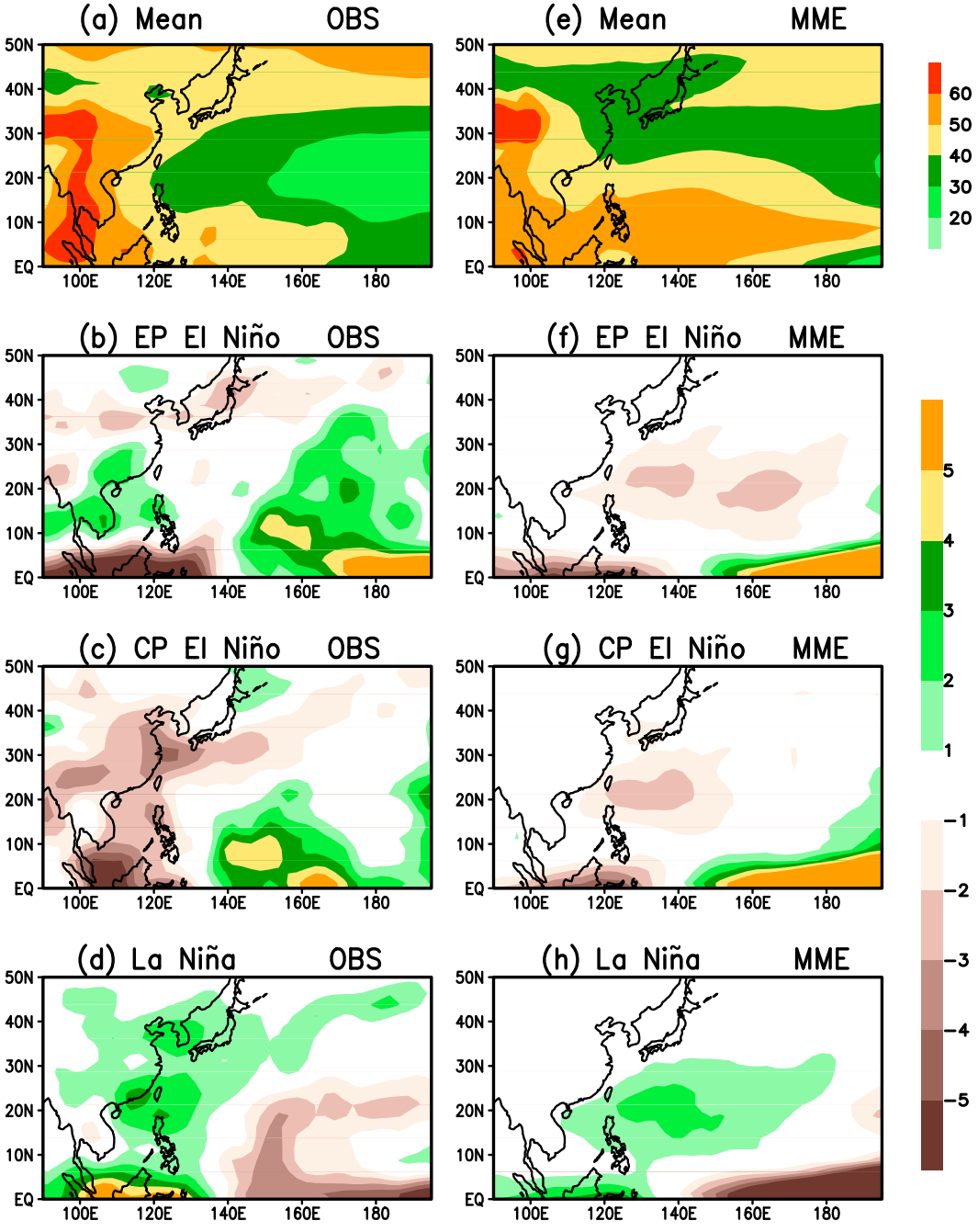

FIG. 13. JASO climatology of 500-hPa relative humidity (%) in (a) observations and (e) the MME mean, and composites of JASO mean 500-hPa relative humidity anomalies (%) for (b),(f) EP El Niño; (c),(g) CP El Niño; and (d),(h) La Niña during 1982–2009 in (b)–(d) the observations and (f)–(h) the MME mean.

analyzed. The results indicate that each model has different mean biases in terms of TC track density and TC origins. Similar to the results of Wang et al. (2014) for the Atlantic basin, among the five models, the GFDL model has the best performance, although it tends to overestimate annual TC numbers. The MME mean is the closest to the observations in terms of climatological annual mean TC numbers and has the smallest RMSE and a relatively high anomaly correlation. Therefore, it is recommended to use the MME for dynamical typhoon seasonal predictions over the WNP.

For the association with ENSO, overall, the GCMs simulate well the variability of WNP TCs, with stronger TC activity during EP and CP El Niños and weaker TC

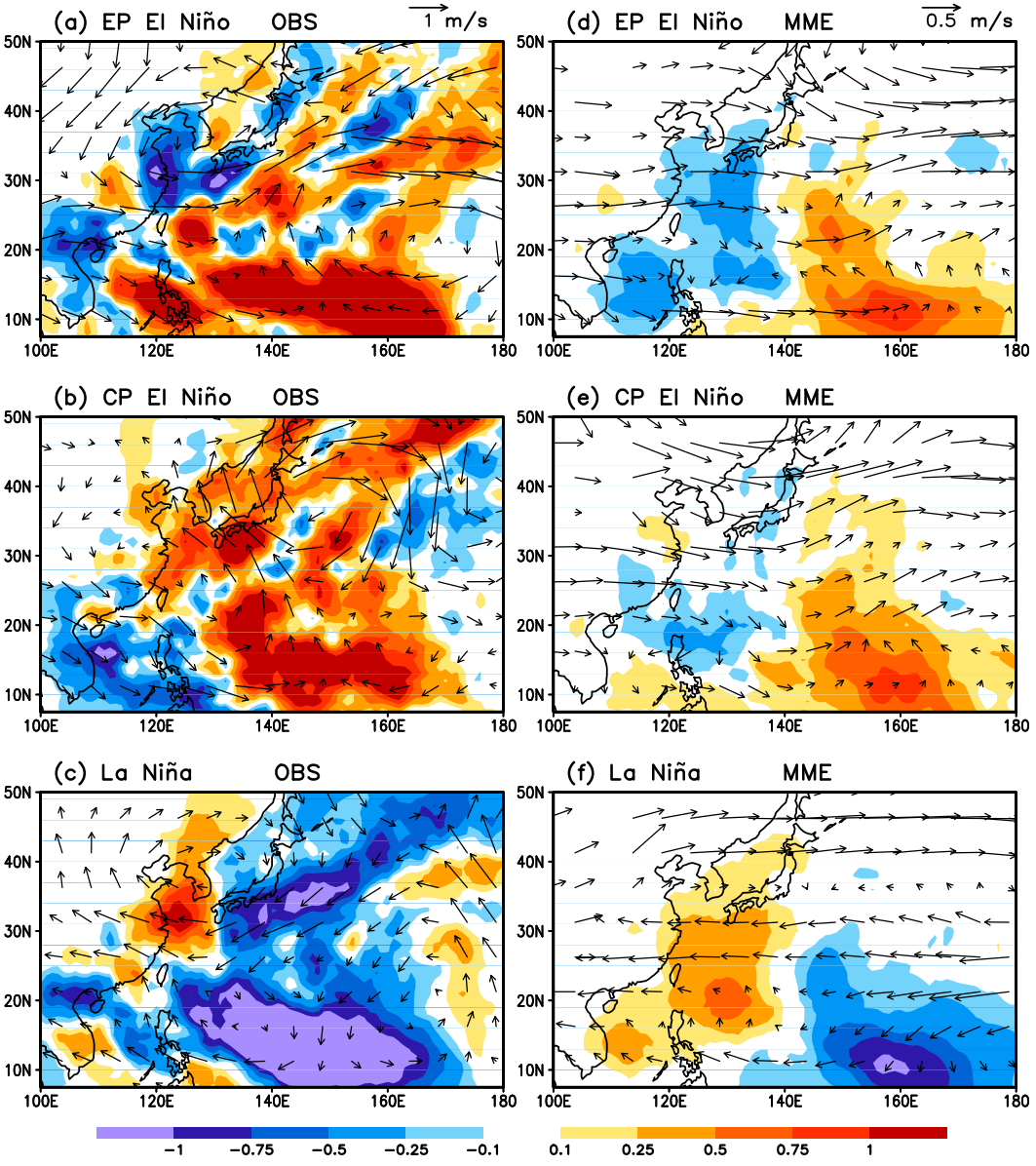

FIG. 14. Composites of JASO mean deep-layer steering flow anomaly (vectors; $m\,s^{-1}$) and TC track density anomaly (shadings) for (a),(d) EP El Niño; (b),(e) CP El Niño; and (c),(f) La Niña during 1982–2009 in (a)–(c) observations and (d)–(f) the MME mean. Arrow scales are given at the top right of (a) and (d) for the observations and MME, respectively.

activity during La Niña. On the other hand, however, GCMs fail to reproduce the observed differences of WNP TC activity between EP and CP El Niños. The spatial distribution of TC track density and origins is not completely consistent among the models, indicating strong model dependence.

The differences between the models and the observations may be associated with the biases of multiple environmental factors affecting TCs. For instance, the majority of the models are unable to simulate the detailed spatial distribution of vertical wind shear in response to the shift in tropical heating associated with CP El Niño. The models also have biases in simulating the ENSO-related variations of the large-scale atmospheric humidity field and deep-layer steering flow, both of which affect TC genesis and the distribution of TC tracks. Specifically, the MME fails to capture the intensity of deep convection anomalies over the Maritime Continent during different ENSO phases, which may be a manifestation

of a key problem causing a lower model skill in the WNP than in the North Atlantic. Furthermore, the small sample sizes for ENSO events in the observations may be a factor affecting the robustness of the composite results.

There are other factors that may affect the results of the simulated interannual variability of TCs. Besides the resolution of the models, two other factors mentioned by Wang et al. (2014) should also be noted here. One is the model sensitivity to different SST datasets (e.g., LaRow 2013). The FSU model is forced with the NOAA OISSTv2, whereas the other models are forced with HadISST. The other is the different TC tracking schemes employed by the five modeling groups for their GCMs (Table 1). TC track density and origins in the models are proved to be sensitive to the schemes used, which has been showed in Horn et al. (2014). Even so, this study indicates that, given a good prediction of ENSO SST in coupled GCMs, certain skills can be achieved for the dynamical seasonal prediction of TC activity over the WNP.

Acknowledgments. Most of this work was finished during a visit by Dr. Han to the Climate Prediction Center, NCEP/NWS/NOAA. This research was jointly supported by the National Basic Research Program of China under Grants 2013CB430203 and 2012CB417205, Key project of National Nature Science Foundation of China under Grant 91437215, the China Meteorological Special Program under Grants GYHY201506013, GYHY201406022, and GYHY201306028, the National Nature Science Foundation of China under Grant 41575090, and the Major International (Regional) Joint Research Project of National Science Foundation of China (41520104008). The authors thank three anonymous reviewers and the editor for their insightful and constructive comments and suggestions.

REFERENCES

Ashok, K., and T. Yamagata, 2009: Climate change: The El Niño with a difference. *Nature*, **461**, 481–484, doi:10.1038/461481a.

——, S. K. Behera, S. A. Rao, H. Weng, and T. Yamagata, 2007: El Niño Modoki and its possible teleconnection. *J. Geophys. Res.*, **112**, C11007, doi:10.1029/2006JC003798.

Buizza, R., P. L. Houtekamer, Z. Toth, G. Pellerin, M. Wei, and Y. Zhu, 2005: A comparison of the ECMWF, MSC, and NCEP global ensemble prediction systems. *Mon. Wea. Rev.*, **133**, 1076–1097, doi:10.1175/MWR2905.1.

Camargo, S. J., and S. E. Zebiak, 2002: Improving the detection and tracking of tropical cyclones in atmospheric general circulation models. *Wea. Forecasting*, **17**, 1152–1162, doi:10.1175/1520-0434(2002)017<1152:ITDATO>2.0.CO;2.

——, and A. H. Sobel, 2005: Western North Pacific tropical cyclone intensity and ENSO. *J. Climate*, **18**, 2996–3006, doi:10.1175/JCLI3457.1.

——, A. G. Barnston, and S. E. Zebiak, 2005: A statistical assessment of tropical cyclone activity in atmospheric general circulation models. *Tellus*, **57A**, 589–604, doi:10.1111/j.1600-0870.2005.00117.x.

——, K. A. Emanuel, and A. H. Sobel, 2007a: Use of a genesis potential index to diagnose ENSO effects on tropical cyclone genesis. *J. Climate*, **20**, 4819–4834, doi:10.1175/JCLI4282.1.

——, A. W. Robertson, S. J. Gaffney, P. Smyth, and M. Ghil, 2007b: Cluster analysis of typhoon tracks. Part II: Large-scale circulation and ENSO. *J. Climate*, **20**, 3654–3676, doi:10.1175/JCLI4203.1.

Capotondi, A., and Coauthors, 2015: Understanding ENSO diversity. *Bull. Amer. Meteor. Soc.*, **96**, 921–938, doi:10.1175/BAMS-D-13-00117.1.

Chan, J. C. L., 2000: Tropical cyclone activity over the western North Pacific associated with El Niño and La Niña events. *J. Climate*, **13**, 2960–2972, doi:10.1175/1520-0442(2000)013<2960:TCAOTW>2.0.CO;2.

——, J. E. Shi, and C. M. Lam, 1998: Seasonal forecasting of tropical cyclone activity over the western North Pacific and the South China Sea. *Wea. Forecasting*, **13**, 997–1004, doi:10.1175/1520-0434(1998)013<0997:SFOTCA>2.0.CO;2.

Chauvin, F., J. F. Royer, and M. Déqué, 2006: Response of hurricane-type vortices to global warming as simulated by ARPEGE-Climat at high resolution. *Climate Dyn.*, **27**, 377–399, doi:10.1007/s00382-006-0135-7.

Chen, G., and C. Y. Tam, 2010: Different impacts of two kinds of Pacific Ocean warming on tropical cyclone frequency over the western North Pacific. *Geophys. Res. Lett.*, **37**, L01803, doi:10.1029/2009GL041708.

Chen, J.-H., and S.-J. Lin, 2011: The remarkable predictability of inter-annual variability of Atlantic hurricanes during the past decade. *Geophys. Res. Lett.*, **38**, L11804, doi:10.1029/2011GL047629.

——, and ——, 2013: Seasonal predictions of tropical cyclones using a 25-km-resolution general circulation model. *J. Climate*, **26**, 380–398, doi:10.1175/JCLI-D-12-00061.1.

Chen, T. C., S. Y. Wang, and M. C. Yen, 2006: Interannual variation of tropical cyclone activity over the western North Pacific. *J. Climate*, **19**, 5709–5720, doi:10.1175/JCLI3934.1.

Cheung, K. K. W., 2004: Large-scale environmental parameters associated with tropical cyclone formations in the western North Pacific. *J. Climate*, **17**, 466–484, doi:10.1175/1520-0442(2004)017<0466:LEPAWT>2.0.CO;2.

Chia, H. H., and C. F. Ropelewski, 2002: The interannual variability in the genesis location of tropical cyclones in the northwest Pacific. *J. Climate*, **15**, 2934–2944, doi:10.1175/1520-0442(2002)015<2934:TIVITG>2.0.CO;2.

Cocke, S., and T. E. LaRow, 2000: Seasonal predictions using a regional spectral model embedded within a coupled ocean–atmospheric model. *Mon. Wea. Rev.*, **128**, 689–708, doi:10.1175/1520-0493(2000)128<0689:SPUARS>2.0.CO;2.

Colbert, A. J., and B. J. Soden, 2012: Climatological variations in North Atlantic tropical cyclone tracks. *J. Climate*, **25**, 657–673, doi:10.1175/JCLI-D-11-00034.1.

Emanuel, K. A., 2007: Environmental factors affecting tropical cyclone power dissipation. *J. Climate*, **20**, 5497–5509, doi:10.1175/2007JCLI1571.1.

Fan, K., and H. Wang, 2009: A new approach to forecasting typhoon frequency over the western North Pacific. *Wea. Forecasting*, **24**, 974–986, doi:10.1175/2009WAF2222194.1.

Graham, N. E., J. Michaelson, and T. P. Barnett, 1987: An investigation of the El Niño–Southern Oscillation cycle with

statistical models: 1. Predictor field characteristics. *J. Geophys. Res.*, **92**, 14 251–14 270, doi:10.1029/JC092iC13p14251.

Gray, W. M., 1979: Hurricanes: Their formation, structure, and likely role in the tropical circulation. *Meteorology over the Tropical Oceans*, D. B. Shaw, Ed., Royal Meteorological Society, 155–218.

Ha, Y., Z. Zhong, and Y. Hu, 2013: Influences of ENSO on western North Pacific tropical cyclone kinetic energy and its meridional transport. *J. Climate*, **26**, 322–332, doi:10.1175/JCLI-D-11-00543.1.

Ho, C.-H., J.-J. Baik, J.-H. Kim, D.-Y. Gong, and C.-H. Sui, 2004: Interdecadal changes in summertime typhoon tracks. *J. Climate*, **17**, 1767–1776, doi:10.1175/1520-0442(2004)017<1767:ICISTT>2.0.CO;2.

Hong, C.-C., Y.-H. Li, T. Li, and M.-Y. Lee, 2011: Impacts of central Pacific and eastern Pacific El Niños on tropical cyclone tracks over the western North Pacific. *Geophys. Res. Lett.*, **38**, L16712, doi:10.1029/2011GL048821.

Horn, M., and Coauthors, 2014: Tracking scheme dependence of simulated tropical cyclone response to idealized climate simulations. *J. Climate*, **27**, 9197–9213, doi:10.1175/JCLI-D-14-00200.1.

Hu, Z.-Z., A. Kumar, B. Jha, W. Wang, B. Huang, and B. Huang, 2012: An analysis of warm pool and cold tongue El Niños: Air–sea coupling processes, global influences, and recent trends. *Climate Dyn.*, **38**, 2017–2035, doi:10.1007/s00382-011-1224-9.

Kanamitsu, M., W. Ebisuzaki, J. Woollen, S.-K. Yang, J. J. Hnilo, M. Fiorino, and G. L. Potter, 2002: NCEP–DOE AMIP-II Reanalysis (R-2). *Bull. Amer. Meteor. Soc.*, **83**, 1631–1643, doi:10.1175/BAMS-83-11-1631.

Kao, H. Y., and J. Y. Yu, 2009: Contrasting eastern Pacific and central Pacific types of ENSO. *J. Climate*, **22**, 615–631, doi:10.1175/2008JCLI2309.1.

Kim, H. M., P. J. Webster, and J. A. Curry, 2009: Impact of shifting patterns of Pacific Ocean warming on North Atlantic tropical cyclones. *Science*, **325**, 77–80, doi:10.1126/science.1174062.

——, ——, and ——, 2011: Modulation of North Pacific tropical cyclone activity by three phases of ENSO. *J. Climate*, **24**, 1839–1849, doi:10.1175/2010JCLI3939.1.

Kim, H.-S., C.-H. Ho, J.-H. Kim, and P.-S. Chu, 2012: Track-pattern-based model for seasonal prediction of tropical cyclone activity in the western North Pacific. *J. Climate*, **25**, 4660–4678, doi:10.1175/JCLI-D-11-00236.1.

Kug, J. S., F. F. Jin, and S. I. An, 2009: Two types of El Niño events: Cold-tongue El Niño and warm-pool El Niño. *J. Climate*, **22**, 1499–1515, doi:10.1175/2008JCLI2624.1.

Lander, M. A., 1994: An exploratory analysis of the relationship between tropical storm formation in the western North Pacific and ENSO. *Mon. Wea. Rev.*, **122**, 636–651, doi:10.1175/1520-0493(1994)122<0636:AEAOTR>2.0.CO;2.

Larkin, N. K., and D. E. Harrison, 2005: On the definition of El Niño and associated seasonal average U.S. weather anomalies. *Geophys. Res. Lett.*, **32**, L13705, doi:10.1029/2005GL022738.

LaRow, T. E., 2013: The impact of SST bias correction on North Atlantic hurricane retrospective forecasts. *Mon. Wea. Rev.*, **141**, 490–498, doi:10.1175/MWR-D-12-00152.1.

——, Y.-K. Lim, D. W. Shin, E. P. Chassignet, and S. Cocke, 2008: Atlantic basin seasonal hurricane simulations. *J. Climate*, **21**, 3191–3206, doi:10.1175/2007JCLI2036.1.

Li, X., S. Yang, H. Wang, X. Jia, and A. Kumar, 2013: A dynamical-statistical forecast model for the annual frequency of western Pacific tropical cyclones based on the NCEP Climate Forecast System version 2. *J. Geophys. Res. Atmos.*, **118**, 12 061–12 074, doi:10.1002/2013JD020708.

McPhaden, M. J., T. Lee, and D. McClurg, 2011: El Niño and its relationship to changing background conditions in the tropical Pacific Ocean. *Geophys. Res. Lett.*, **38**, L15709, doi:10.1029/2011GL048275.

Mei, W., S. Xie, M. Zhao, and Y. Wang, 2015: Forced and internal variability of tropical cyclone track density in the western North Pacific. *J. Climate*, **28**, 143–167, doi:10.1175/JCLI-D-14-00164.1.

Molod, A., L. Takacs, M. Suarez, J. Bacmeister, I.-S. Song, and A. Eichmann, 2012: The GEOS-5 Atmospheric General Circulation Model: Mean climate and development from MERRA to Fortuna. NASA Tech. Rep. NASA/TM-2012-104606, Vol. 28, 117 pp. [Available online at http://gmao.gsfc.nasa.gov/pubs/docs/tm28.pdf.]

Murakami, H., and Coauthors, 2015: Simulation and prediction of category 4 and 5 hurricanes in the high-resolution GFDL HiFLOR Coupled Climate Model. *J. Climate*, **28**, 9058–9079, doi:10.1175/JCLI-D-15-0216.1.

Rayner, N. A., D. E. Parker, E. B. Horton, C. K. Folland, L. V. Alexander, D. P. Rowell, E. C. Kent, and A. Kaplan, 2003: Global analyses of sea surface temperature, sea ice, and night marine air temperature since the late nineteenth century. *J. Geophys. Res.*, **108**, 4407, doi:10.1029/2002JD002670.

Ren, F., J. Liang, G. Wu, W. Dong, and X. Yang, 2011: Reliability analysis of climate change of tropical cyclone activity over the western North Pacific. *J. Climate*, **24**, 5887–5898, doi:10.1175/2011JCLI3996.1.

Reynolds, R. W., N. A. Rayner, T. M. Smith, D. C. Stokes, and W. Wang, 2002: An improved in situ and satellite SST analysis for climate. *J. Climate*, **15**, 1609–1625, doi:10.1175/1520-0442(2002)015<1609:AIISAS>2.0.CO;2.

Rienecker, M. M., and Coauthors, 2008: The GEOS-5 Data Assimilation System—Documentation of versions 5.0.1, 5.1.0, and 5.2.0. NASA Tech. Rep. NASA/TM-2008-104606, Vol. 27, 92 pp. [Available online at http://gmao.gsfc.nasa.gov/pubs/docs/Rienecker369.pdf.]

Schmidt, G. A., and Coauthors, 2014: Configuration and assessment of GISS ModelE2 contributions to the CMIP5 archive. *J. Adv. Model. Earth Syst.*, **6**, 141–184, doi:10.1002/2013MS000265.

Scoccimarro, E., and Coauthors, 2011: Effects of tropical cyclones on ocean heat transport in a high-resolution coupled general circulation model. *J. Climate*, **24**, 4368–4384, doi:10.1175/2011JCLI4104.1.

Shaevitz, D. A., and Coauthors, 2014: Characteristics of tropical cyclones in high-resolution models in the present climate. *J. Adv. Model. Earth Syst.*, **6**, 1154–1172, doi:10.1002/2014MS000372.

Takahashi, K., A. Montecinos, K. Goubanova, and B. Dewitte, 2011: ENSO regimes: Reinterpreting the canonical and Modoki El Niño. *Geophys. Res. Lett.*, **38**, L10704, doi:10.1029/2011GL047364.

Vecchi, G. A., and Coauthors, 2014: On the seasonal forecasting of regional tropical cyclone activity. *J. Climate*, **27**, 7994–8016, doi:10.1175/JCLI-D-14-00158.1.

von Storch, H. V., and F. W. Zwiers, 1999: *Statistical Analysis in Climate Research*. Cambridge University Press, 496 pp.

Walsh, K. J. E., and Coauthors, 2015: Hurricanes and climate: The U.S. CLIVAR Working Group on Hurricanes. *Bull. Amer. Meteor. Soc.*, **96**, 997–1017, doi:10.1175/BAMS-D-13-00242.1.

Wang, B., and J. C. L. Chan, 2002: How strong ENSO events affect tropical storm activity over the western North Pacific. *J. Climate*, **15**, 1643–1658, doi:10.1175/1520-0442(2002)015<1643:HSEEAT>2.0.CO;2.

Wang, C., C. Li, M. Mu, and W. Duan, 2013: Seasonal modulations of different impacts of two types of ENSO events on tropical cyclone activity in the western North Pacific. *Climate Dyn.*, **40**, 2887–2902, doi:10.1007/s00382-012-1434-9.

Wang, H., J. K. E. Schemm, A. Kumar, W. Wang, L. Long, M. Chelliah, G. D. Bell, and P. Peng, 2009: A statistical forecast model for Atlantic seasonal hurricane activity based on the NCEP dynamical seasonal forecast. *J. Climate*, **22**, 4481–4500, doi:10.1175/2009JCLI2753.1.

——, A. Kumar, W. Wang, and B. Jha, 2012: U.S. summer precipitation and temperature patterns following the peak phase of El Niño. *J. Climate*, **25**, 7204–7215, doi:10.1175/JCLI-D-11-00660.1.

——, and Coauthors, 2014: How well do global climate models simulate the variability of Atlantic tropical cyclones associated with ENSO? *J. Climate*, **27**, 5673–5692, doi:10.1175/JCLI-D-13-00625.1.

Xie, P., and P. A. Arkin, 1997: Global precipitation: A 17-year monthly analysis based on gauge observations, satellite estimates, and numerical model outputs. *Bull. Amer. Meteor. Soc.*, **78**, 2539–2558, doi:10.1175/1520-0477(1997)078<2539:GPAYMA>2.0.CO;2.

Yeh, S. W., J. S. Kug, B. Dewitte, M. H. Kwon, B. P. Kirtman, and F. F. Jin, 2009: El Niño in a changing climate. *Nature*, **461**, 511–514, doi:10.1038/nature08316.

Yonekura, E., and T. M. Hall, 2011: A statistical model of tropical cyclone tracks in the western North Pacific with ENSO-dependent cyclogenesis. *J. Appl. Meteor. Climatol.*, **50**, 1725–1739, doi:10.1175/2011JAMC2617.1.

Zhang, H., and Y. Guan, 2014: Impacts of four types of ENSO events on tropical cyclones making landfall over mainland China based on three best-track datasets. *Adv. Atmos. Sci.*, **31**, 154–164, doi:10.1007/s00376-013-2146-8.

Zhao, M., I. M. Held, S.-J. Lin, and G. A. Vecchi, 2009: Simulations of global hurricane climatology, interannual variability, and response to global warming using a 50-km resolution GCM. *J. Climate*, **22**, 6653–6678, doi:10.1175/2009JCLI3049.1.

——, ——, and G. A. Vecchi, 2010: Retrospective forecasts of the hurricane season using a global atmospheric model assuming persistence of SST anomalies. *Mon. Wea. Rev.*, **138**, 3858–3868, doi:10.1175/2010MWR3366.1.